

Accretion-modified stellar-mass black hole distribution and milli-Hz gravitational wave backgrounds from galaxy centre

Mengye Wang,¹ Yiqiu Ma,^{2*} and Qingwen Wu,^{1†}

¹Department of Astronomy, School of physics, Huazhong University of Science and Technology, Luoyu Road 1037, Wuhan, China

²centre for Gravitational Experiment, Hubei Key Laboratory of Gravitation and Quantum Physics, School of physics, Huazhong University of Science and Technology, Luoyu Road 1037, Wuhan, China

Accepted XXX. Received YYY; in original form ZZZ

ABSTRACT

Gas accretion of embedded stellar-mass black holes (sBHs) or stars in the accretion disk of active galactic nuclei (AGNs) will modify the mass distribution of these sBHs and stars, which will also affect the migration of the sBHs/stars. With the introduction of the mass accretion effect, we simulate the evolution of the sBH/star distribution function in a consistent way by extending the Fokker-Planck equation of sBH/star distributions to the mass-varying scenario, and explore the mass distribution of sBHs in the nuclear region of the galaxy centre. We find that the sBHs can grow up to several tens solar mass and form heavier sBH binaries, which will be helpful for us to understand the black-hole mass distribution as observed by the current and future ground-based gravitational wave detectors (e.g., LIGO/Virgo, ET and Cosmic Explorer). We further estimate the event rate of extreme mass-ratio inspirals (EMRI) for sBH surrounding the massive black hole and calculate the stochastic gravitational wave (GW) background of the EMRIs. We find that the background can be detected in future space-borne GW detectors after considering the sBHs embedded in the AGN disk, while the mass accretion has a slight effect on the GW background.

Key words: black hole physics– accretion– accretion disk – EMRI – gravitational wave

1 INTRODUCTION

Stellar-mass binary black holes (BBH) are one of the main target sources for the ground-based gravitational wave (GW) detectors such as LIGO, Virgo and KAGRA (LIGO Scientific Collaboration et al. 2015; Acernese et al. 2015; Kagra Collaboration et al. 2019). More than 90 stellar-mass BBH merging events have been detected by Advanced LIGO and Advanced Virgo (The LIGO Scientific Collaboration et al. 2021a; Acernese et al. 2015), which opens the era of GW astronomy. Currently detected events indicate a merger rate R to be about $17.3 - 45 \text{ Gyr}^{-3} \text{ yr}^{-1}$ (e.g., The LIGO Scientific Collaboration et al. 2021b; Tiwari & Fairhurst 2021). Increasing BBH merger events detected by the GW detectors provides an opportunity to explore the formation channels of these BBHs (Kinugawa et al. 2021; Chattopadhyay et al. 2022; Ford & McKernan 2021).

Two main BBH formation channels are proposed, which are the isolated evolution of massive binaries in galactic fields (e.g., Belczynski et al. 2016; Kinugawa et al. 2021) and the dynamical evolution in dense stellar environments (e.g., Stone et al. 2017; Yang et al. 2019b; Chatterjee et al. 2017; McKernan et al. 2018; Mandel & Farmer 2022; Li et al. 2022; Li & Lai 2022; Samsing et al. 2022). Strong observational evidence shows that the massive galaxies host massive black holes (MBH) in their centre (e.g., Kormendy & Ho 2013), where the MBH mass range from $\sim 10^5 - 10^{10} M_{\odot}$. The MBH can grow via accreting the surrounding gas and form an ac-

cretion disk, which generates an active galactic nuclear (AGN). For an optically thick, geometrically thin standard AGN disk (Shakura & Sunyaev 1973), gravitational instability happens at the outer region with several thousand gravitational radii, leading to the star formation via the fragmentation of the gas (e.g., Sirko & Goodman 2003). Furthermore, some stars in the nuclear star cluster can also be captured into the accretion disk as a result of momentum and energy loss during the star-disk interaction (e.g., Artymowicz 1993; Vilko-viskij & Czerny 2002; McKernan et al. 2012; Kennedy et al. 2016; Panamarev et al. 2018; MacLeod & Lin 2020). These disk stars will evolve quickly due to the possible fast accretion of the gas in the AGN accretion disk (e.g., so-called "accretion-modified star", Wang et al. 2021) and thereby forming compact objects such as stellar-mass black holes (sBHs). These sBHs, together with the sBHs directly captured from the nuclear star cluster by the disk, will migrate inward to the central MBH (e.g., Vilko-viskij & Czerny 2002; McKernan et al. 2012, 2014; Kennedy et al. 2016; Panamarev et al. 2018; Pan & Yang 2021a; Pan et al. 2022). The migration of these sBHs and stars will not only be affected by the centre MBH but also by the interaction with the accretion disk (e.g., Goldreich & Tremaine 1979, 1980; Tanaka et al. 2002; Tanaka & Ward 2004; Fabj et al. 2020; Nasim et al. 2020; Secunda et al. 2019, 2020; Tagawa et al. 2020). The binary system consisting of a sBH and a centre MBH is an important target source of the future space-borne GW detectors (such as LISA/Tianqin/Taiji, Luo et al. 2016; Luo et al. 2020; Robson et al. 2019), which is called Extreme-Mass-Ratio-Inspiral (EMRI) system. There are two main channels for the formation of EMRIs, which are called dry EMRI and wet EMRI. The

*E-mail: myqphy@hust.edu.cn

†E-mail: qwwu@hust.edu.cn

dry EMRIs are mainly produced by multi-body scatterings within the nuclear star cluster and the gravitational capture (such as Hills mechanism, see [Hills 1988](#)), while the wet EMRIs are the EMRIs in a gas-rich environment (e.g., [Pan et al. 2021](#)). For the wet EMRIs, the distributions of nearby stars and sBHs are significantly affected by the dense environments (e.g., [Vilkoviskij & Czerny 2002](#); [McKernan et al. 2012](#); [Kennedy et al. 2016](#); [Panamarev et al. 2018](#); [Pan et al. 2021, 2022](#)). The wet EMRI rate will be significantly increased compared to the dry EMRI rate (e.g., [Pan & Yang 2021a](#)).

The stars/sBHs embedded in the AGN disk can grow quickly due to the accretion effect. This phenomenon has been considered to explain some unexpected massive binary merger events (e.g., GW190521, [Abbott et al. 2020](#)). The stars and stellar-mass compact objects will also accrete and grow quickly in this dense environment, which will lead to their fast evolution (e.g., [Yang et al. 2014](#); [McKinney et al. 2014](#); [Pan & Yang 2021b](#)). It should be noted that current simulations for the evolution of the sBH/star distribution function does not consistently involve the accretion effect, that is, the distribution function evolution does not describe the redistribution of the population among different masses. In this work, we re-examine how mass accretion influences the distribution function evolution through more consistent simulations, which are based on the extended Fokker-Planck equations to the mass varying scenario. Moreover, we also phenomenologically take into account the fact that some main sequence stars will collapse into sBHs when their mass exceeds the gravitational limit in our simulations.

The tools for analysing the distribution functions are based on non-equilibrium statistical mechanics, where we consider the stellar objects in the galaxy as interacting gas particles. The sBHs near the galaxy centre interact mutually, with other stars, and also with the MBH of the galaxy centre. From a mean field point of view, these sBHs (together with the main sequence stars and other compact stars) feel a background gravitational potential created collectively by all the matters in the galaxy, upon which these sBHs/stars are also interacting mutually via gravitational scattering. This system is similar to a collection of mutually interacting particles evolving in an external potential, which must satisfy the Fokker-Planck equation (e.g., [Lightman & Shapiro 1977](#); [Shapiro & Marchant 1978](#); [Cohn & Kulsrud 1978](#); [Cohn 1979](#); [Amaro-Seoane & Preto 2011](#); [Stone et al. 2017, 2018](#)). This means that, in the phase space, the distribution of these particles will evolve due to the advection and also the interaction-induced diffusion. This non-equilibrium statistical mechanics theory has been applied to analyse the star distribution in a galaxy in the 1970s by [Cohn \(1979\)](#).

Investigation of the accretion effect on the sBH mass distribution and possible GW sources of BBHs in the galaxy centre could be a topic that relates to the GW observation at different frequency bands (i.e. multi-band GW astronomy). By simulating the evolution of the sBH distribution via these extended Fokker-Planck equations, this work is devoted to analyse the following problems.

(1) The effect of accretion on the sBH mass distribution near the MBH. Future 3rd generation *ground-based* GW detectors are designed to detect nearly all the stellar-mass binary compact objects in the universe ([Abbott et al. 2017](#); [Maggiore et al. 2020](#)). The effect of accretion studied in this work could be finally tested by the statistics on the properties of these sBH binary systems, which are relevant to their formation history.

(2) The EMRI events, which is an important target source of the proposed *space-borne* gravitational waves detectors such as LISA, Tianqin and Taiji. The accretion process of sBHs in the AGN disk will affect the sBH mass distribution and the EMRI event rate. Therefore, it could potentially affect the observation of the GW

background emitted from the EMRIs in the gas-rich environment by future space-borne GW detectors. In this work, the effect of the accretion on the EMRI rate and the stochastic GW background (GWB) from the EMRIs will be discussed.

This paper is organized as follows. We present the extended Fokker-Planck equations by considering the mass variation effect in Section 2; The simulation setup and simulation results are shown in Sections 3 and 4, respectively; The effect of accretion on the distribution of sBHs, together with its possible connection to the gravitational wave detection using ground-based detectors is investigated in Section 5; In Sections 6 and 7, taking into account the accretion effect, we study the EMRI event rate, the stochastic GWB from these EMRIs, and the observational consequence of the space-borne detectors. Discussions and conclusions are given in Section 8.

2 FOKKER-PLANCK EQUATION WITH VARYING MASS

2.1 Extended Fokker-Planck equation

To include the mass variation effect in the evolution of the distribution function, we extend the original phase space (E, J) with an additional dimension to the phase space (E, J, m) , where the parameters E and J are the orbital energy per unit mass (specific orbital energy) and the orbital angular momentum per unit mass (specific angular momentum). The additional dimension counts the mass variation. Therefore, the new distribution function in the phase space $f(E, J, m)$ is proportional to $dN/(dE dJ dm)$, where dN is the number of particles within $(E, E + dE)$, $(J, J + dJ)$ and $(m, m + dm)$. The Boltzmann equation in this new phase space is:

$$\frac{\partial f(E, J, m)}{\partial t} + \nabla \cdot [f(E, J, m)\mathbf{v}] = \text{collision terms}, \quad (1)$$

where $\nabla = (\partial_E, \partial_J, \partial_m)$. We also have $\mathbf{v} = (\dot{E}, \dot{J}, \dot{m})$, which is only affected by the mean-field background gravitational potential of the galaxy, and the accretion rate of the stars and sBHs. Compared to the previous result obtained in [Lightman & Shapiro \(1977\)](#); [Shapiro & Marchant \(1978\)](#); [Cohn \(1979\)](#); [Merritt \(2013\)](#); [Stone et al. \(2018\)](#); [Pan & Yang \(2021a\)](#); [Broggi et al. \(2022\)](#), the resulting Fokker-Planck equation will have one more term that relates to the mass variation, while other terms would be the same or a straightforward extension of the equations in [Cohn \(1979\)](#). Following the conventions of [Cohn \(1979\)](#), we re-parametrize the phase space as (E, \mathcal{R}) with $\mathcal{R} \equiv J^2/J_c^2$, where $J_c = GM_\bullet \sqrt{1/2E}$ is the specific orbital angular momentum of a sBH with specific energy E on a circular orbit and the M_\bullet is the mass of centre massive black hole (MBH). Given initial distributions of stars and sBHs $f_{s/\text{sBH}}(t = 0, E, \mathcal{R}, m)$, their evolution is governed by the orbit-averaged Fokker-Planck equation

$$\mathcal{C} \frac{\partial f}{\partial t} = -\frac{\partial}{\partial E} F_E - \frac{\partial}{\partial \mathcal{R}} F_{\mathcal{R}} - \mathcal{C} \frac{\partial}{\partial m} (f\dot{m}), \quad (2)$$

where \mathcal{C} is the weighting function defined through $\mathcal{C}(E, \mathcal{R}) \equiv 4\pi^2 P(E, \mathcal{R}) J_c^2(E)$, $P(E, \mathcal{R})$ is the orbital period and $F_{E, \mathcal{R}}$ is the flux given by ([Shapiro & Marchant 1978](#); [Cohn & Kulsrud 1978](#)):

$$F_E = -\left(D_{EE} \frac{\partial f}{\partial E} + D_{E\mathcal{R}} \frac{\partial f}{\partial \mathcal{R}} + D_{E\dot{m}} f \right), \quad (3)$$

$$F_{\mathcal{R}} = -\left(D_{\mathcal{R}\mathcal{R}} \frac{\partial f}{\partial \mathcal{R}} + D_{E\mathcal{R}} \frac{\partial f}{\partial E} + D_{\mathcal{R}\dot{m}} f \right).$$

The terms with diffusion coefficients $(D_{EE}, D_{E\mathcal{R}}, D_{\mathcal{R}\mathcal{R}})$ represent the relaxation of the particles in the phase space due to the energy

and angular momentum exchange induced by gravitational interaction. We assume that the accretion process is not stochastic and the mass increase of the sBHs and stars is steady, therefore there is no direct participation of the accretion process in the diffusion. The $(D_E, D_{\mathcal{R}})$ terms, together with the m -derivative term in equation (2) are the advection coefficients, where the $(D_E, D_{\mathcal{R}})$ terms describe the advection due to the energy and angular momentum increment in the process of two-body scattering. The m -derivative term in equation (2) describes the advection in the m -direction through accretion. However, mass accretion indirectly affects the diffusion process in the (E, \mathcal{R}) directions. This is because the gravitational two-body scattering, which is the source of the diffusion process, depends on the mass of the encountering particles. This can be naturally extended in the following way. For example, the diffusion in the energy direction now can be rewritten as:

$$D_{EE}(E, \mathcal{R}, m) = \frac{8\pi^2}{3} J_c^2 \int dm' \int_{r_-}^{r_+} \frac{dr}{v_r} v^2 [F_0(m', E, r) + F_2(m', E, r)],$$

with

$$F_0(m, E, r) = (4\pi)^2 G m^2 \ln \Lambda \int_{-\infty}^E dE' \bar{f}(m, E'),$$

$$F_2(m, E, r) = (4\pi)^2 G m^2 \ln \Lambda \int_E^{\phi(r)} dE' \left(\frac{\phi - E'}{\phi - E} \right)^{3/2} \bar{f}(m, E'),$$
(4)

where r_+/r_- is the orbiters' apocentre/pericenter radius, v_r is the radial velocity, $\bar{f}(m, E) = \int d\mathcal{R} f(m, E, \mathcal{R})$, $\ln \Lambda = 10$ is the Coulomb's logarithm (Binney & Tremaine 2008; Amaro-Seoane 2018) and $\phi(r)$ is the gravitational potential defined in equation (9). The other diffusion coefficients can be extended similarly, as listed in Appendix A. In the later simulation, the particles will be grouped in terms of mass to discretize these differential equations.

When the MBH has an accretion disk, the above diffusion and advection coefficients will be affected by the accretion disk. The star-disk interaction can excite the density wave (Goldreich & Tremaine 1979, 1980; Tanaka et al. 2002; Tanaka & Ward 2004), which will speed up the migration of stars/sBHs. This migration process is driven by the star-disk interaction, thereby being a deterministic process if the accretion disk has a steady structure. Therefore, the interaction between the accretion disk and the stars/sBHs will mostly affect the advection term (see Section 3 for details), while the diffusion terms are still determined by the random gravitational scattering between the stars/sBHs (see also, Pan & Yang 2021a).

2.2 sBH/star accretion in the AGN disk

Generally speaking, the accretion process of sBHs in AGN disk is affected by many factors and therefore is quite complicated (e.g., Wang et al. 2021). The widely adopted Bondi accretion model is over-simplified and many physical effects should be taken into account, such as radiative feedback, vertical stratification, shear viscosity, tidal effects and gap opening, etc. Yang et al. (2014) and McKinney et al. (2014) have studied the two- and three-dimensional general relativistic radiation magnetohydrodynamical simulation of super-Eddington accretion. Moreover, Pan & Yang (2021b) studied the supercritical accretion of stellar-mass compact objects in the AGN disk using a general relativistic framework, which considered both the inflow and outflow. Their results suggested that the sBHs' accretion rate is roughly $\sim 10\dot{M}_{\text{Edd}}$ even if the inflow rate at the outer edge of the sBH accretion disk is very high. Considering the disk wind under super-Eddington accretion, it is found that the in-

trinsic accretion rate is limited to several times of Eddington rate (e.g., Dotan & Shaviv 2011; Gu 2012; Feng et al. 2019). In the outer region, the disk is unstable so that it could be fragmentation and collapse into clumps (Sirko & Goodman 2003; Durisen et al. 2007; Derdzinski & Mayer 2022). In this way, there may not be enough gas for accretion in the outer unstable region. In this work, we set the accretion rate of sBHs in AGN disk as a free parameter, which ranges from several to several tens Eddington accretion rate (\dot{M}_{Edd}) in the inner stable region and equal to \dot{M}_{Edd} if the sBH stay in the outer unstable region.

The main sequence stars usually have a higher accretion rate than the sBH. Similarly, it is still a lack of a sufficiently clear understanding of the detailed accretion process owing to the complexities of stellar feedback (radiation and winds) and its impacts on the disk structure (Cantiello et al. 2021; Dittmann et al. 2021; Jermyn et al. 2021). In the stable region of the AGN disk, to avoid numerous uncertainties in the modeling of those effects, we use the following accretion model fit by the top-heavy stellar mass distribution, which is inferred from the universally high abundance ratio of [Fe/Mg] (Toyouchi et al. 2022),

$$\dot{m}_s = \dot{M}_{0.1} \left(\frac{m_s}{0.1M_{\odot}} \right)^2 \left(1 + \frac{m_s}{M_c} \right)^{\alpha-2},$$
(5)

where M_c , α and $\dot{M}_{0.1}$ are three tunable parameters (see Table 1 in Toyouchi et al. 2022). Here, we adopt the model B in Toyouchi et al. (2022), where the parameters are $\dot{M}_{0.1} = 2.3 \times 10^{-8} M_{\odot} \text{yr}^{-1}$, $M_c = 9.4 M_{\odot}$, $\alpha = -0.5$ and the maximum star mass $M_{\text{max}} = 300 M_{\odot}$. We also assume $\dot{m}_s = \dot{M}_{\text{Edd}}$ in the unstable region of the AGN disk. With increasing masses, some main sequence stars will collapse and become sBHs, if the orbits of these stars are lying on the accretion disk of the centre MBH. It means that there will be a source term in equation (2) for the sBH distribution on the accretion disk, as we shall present more carefully in the next section.

The gas in the accretion process is supplied by the dense disk environment in the AGNs. However, the active galaxies may have duty cycles (e.g., Shulevski et al. 2015; Turner 2018), that is, the MBH is only active in some stages, where the accretion disk of the central MBH will diminish during its quiet stage. In the following simulation, we assume that the mass of stars and sBHs remains unchanged during the quiet stage, and turn on the \dot{m} in the Fokker-Planck equation only when the galaxy is in its active stage.

3 SIMULATION SETUP

We consider the following two-stage physical scenario. Given the initial distribution function of the star and sBH in the nuclear region of galaxies, we first simulate the star/sBH distribution function for 5 Gyr in the quiet stage of the galaxy, without the participation of the centre MBH's accretion disk. In this quiet stage, the evolution is spherically symmetric. After that, we turn on the accretion disk when the galaxy enters its active stage. In this active stage, the plane of the accretion disk corresponding to the latitude angle $\theta = \pi/2$ becomes specific, and the spherical symmetry of the evolution will break. The general framework of the numerical method is based on the work of Pan & Yang (2021a); Broggi et al. (2022).

3.1 Quiet stage evolution

In the quiet stage, the standard Fokker-Planck equations are given in the literature (e.g., Cohn & Kulsrud 1978; Cohn 1979), i.e., set the accretion rate $\dot{m}_{s/\text{sBH}} = 0$ of stars/sBHs in equation (2). We set the

initial and boundary condition following Tremaine’s MBH+stellar cluster model (Tremaine et al. 1994).

The stars in the stellar cluster are assumed to have a single mass component with $m_s = 1M_\odot$, while the mass of sBH in the stellar cluster is distributed within $m_{\text{sBH}} = 5 - 15M_\odot$. The total mass of stars is fixed to be $M_s = 20M_\bullet$ (see also, Pan & Yang 2021a; Broggi et al. 2022), where M_\bullet is the mass of the central MBH and the total mass of sBHs is denoted as M_{sBH} . In Tremaine’s cluster model, the initial number densities of stars and sBHs with different masses are given by (see also, Binney & Tremaine 2008):

$$n_s(m_s, r) = \frac{M_s}{m_s} \frac{3 - \gamma}{4\pi} \frac{r_a}{r^\gamma (r + r_a)^{4 - \gamma}} \delta(m_s - M_\odot), \quad (6)$$

$$n_{\text{sBH}}(m_{\text{sBH}}, r) = \varphi(m_{\text{sBH}}) \times n_s(r),$$

where $r_a = 4GM_\bullet/\sigma_*^2 \equiv 4r_h$ is the radius of density transition (r_h is the influential radius of the MBH with mass M_\bullet), σ_* is the stellar velocity dispersion given by $M_\bullet - \sigma_*$ relation (Tremaine et al. 2002; Gültekin et al. 2009),

$$M_\bullet = 1.53 \times 10^6 M_\odot \left(\frac{\sigma_*}{70 \text{ km/s}} \right)^{4.24} \quad (7)$$

and $\gamma \sim 1.2 - 1.8$ is the density scaling power index (Tremaine et al. 1994; Binney & Tremaine 2008). The $\varphi(m_{\text{sBH}}) \propto m_{\text{sBH}}^{-2.35}$ (Salpeter 1955) is the relative abundance of sBHs with different mass and $n_s(r) \equiv \int n_s(m_s, r) dm_s$ is the total number density of the stars. The total relative abundance of sBHs is defined as

$$\varphi = \int_{5M_\odot}^{15M_\odot} \varphi(m_{\text{sBH}}) dm_{\text{sBH}}, \quad (8)$$

of which the value is assumed to be 0.001 – 0.002 in Pan & Yang (2021a).

With the above density profiles, the collective gravitational potential background can be derived as:

$$\phi(r) = \frac{GM_\bullet}{r} + \frac{G(M_s + M_{\text{sBH}})}{r_a} \frac{1}{2 - \gamma} \left[1 - \left(\frac{r}{r + r_a} \right)^{2 - \gamma} \right]. \quad (9)$$

In this case, the initial distribution function in the (E, \mathcal{R}, m) -phase space is (Tremaine et al. 1994; Binney & Tremaine 2008)

$$f_{s/\text{sBH}}(t = 0, E, \mathcal{R}, m_{s/\text{sBH}}) = \frac{\sqrt{2}}{(2\pi)^2} \frac{d}{dE} \int_0^E \frac{dn_{s/\text{sBH}}}{d\phi} \frac{d\phi}{\sqrt{E - \phi}}, \quad (10)$$

where $n_{s/\text{sBH}}$ is the number density of stars/sBHs (see equation (6)).

The boundary conditions are set as follows, which is widely adopted in literature (e.g., Cohn & Kulsrud 1978; Cohn 1979; Merritt 2013; Pan & Yang 2021a; Broggi et al. 2022):

(1) At $E = 0$ where the stars and sBHs are distributed far away from the central MBH, their long relaxation time allows us to assume the distribution function to be independent of time and equal to the initial distributions.

(2) The boundary $\mathcal{R} = 1$ (or equivalently $J = J_c(E)$) corresponds to circular orbits, which defines the edge of the phase space in the \mathcal{R} -direction. Therefore, the flux in the R -direction should vanish for both stars and sBHs, i.e. $F_{\mathcal{R}}^{s/\text{sBH}}|_{\mathcal{R}=1} = 0$.

(3) At loss-cone boundary $\mathcal{R} = \mathcal{R}_{\text{lc}}(E)$, the behaviour of $f_{s/\text{sBH}}$ has been derived by Cohn and Kulsrud in Cohn (1979) and Merritt (2013) as

$$f_{s/\text{sBH}}(\mathcal{R}) \approx f_{s/\text{sBH}}(\mathcal{R}_{\text{lc}}) \left(1 + \frac{\ln(\mathcal{R}/\mathcal{R}_{\text{lc}})}{\ln(\mathcal{R}_{\text{lc}}/\mathcal{R}_0)} \right), \quad \mathcal{R} \rightarrow \mathcal{R}_{\text{lc}}, \quad (11)$$

where R_0 is given by the following approximate relation

$$\mathcal{R}_0 \approx \mathcal{R}_{\text{lc}} \exp \left(-\sqrt[4]{q^4 + q^2} \right), \quad (12)$$

with

$$q = \frac{1}{4\pi^2 J_c^2 \mathcal{R}_{\text{lc}}} \lim_{\mathcal{R} \rightarrow \mathcal{R}_{\text{lc}}} \frac{D_{\mathcal{R}\mathcal{R}}}{\mathcal{R}}. \quad (13)$$

The limit at a given value of E is numerically performed by evaluating the quantity q at the first grid point above the loss-cone curve.

3.2 Disk-star/sBH Interactions

In the active stage, we adopt the standard thin α -disk model for the stable region of accretion disk (Shakura & Sunyaev 1973). The outer parts of the accretion disk will be prone to unstable if Toomre’s stability parameter Q satisfies:

$$Q \equiv \frac{c_s \Omega}{\pi G \Sigma} \approx \frac{\Omega^2}{2\pi G \rho} < 1. \quad (14)$$

Here, we accept the SG-disk model which maintains a minimum value of the Toomre’s parameter $Q = 1$ by external feed-back heating in the outer region (Sirko & Goodman 2003), which basically means that the disk outer boundary will extend further. The sBH-disk interactions have been discussed in many papers (see Kley & Nelson 2012; Papaloizou 2021; Paardekooper et al. 2022, for reviews), which are briefly summarised as follows.

Type I migration—The periodic orbital motion of sBHs around the MBH excites the density waves, which consist of three components: regular density waves excited by the circular orbit, eccentricity waves excited by the non-circular orbit and bending waves excited by the orbit normal to the disk (e.g., Goldreich & Tremaine 1978, 1980; Tanaka et al. 2002; Tanaka & Ward 2004). The regular density waves exert a (type-I) migration torque on the sBH and drive its migration in the radial direction with the timescale $\tau_{\text{mig,I}}$; the eccentricity and bending density waves damp the orbit eccentricity and the inclination angle to the disk plane on the timescale τ_{wave} . The type-I migration torque can be formulated as (Tanaka et al. 2002; Tanaka & Ward 2004)

$$J_{\text{mig,I}} = C_I \frac{m_{\text{sBH}}}{M} \frac{\Sigma}{M} \frac{r^4 \Omega^2}{h^2}, \quad (15)$$

where $M = M(< r)$ is the total mass consisting of the MBH, stars, sBHs and the disk gas within the radius r , $C_I = -0.85 + d \log \sigma_*/d \log r + 0.9 d \log T_c/d \log r$, $\sigma_*(r)$, $T_c(r)$, $h(r) = H(r)/r$, $\Omega(r)$ are the disk surface density, the disk middle plane temperature, the disk aspect ratio ($H(r)$ is the thickness of the disk at radius r) and the sBH angular velocity, respectively (Paardekooper et al. 2011). The damping timescale of the orbit eccentricity and the inclination is

$$\tau_{\text{wave}} \approx h^2 \tau_{\text{mig,I}} = h^2 \frac{J}{J_{\text{mig,I}}} \sim \frac{M}{m_{\text{sBH}}} \frac{M}{\Sigma r^2} \frac{h^4}{\Omega}, \quad (16)$$

where $J = r^2 \Omega$ is the specific angular momentum of sBH.

Type II migration—The type-I migration is replaced by type-II if the sBH is so massive that a gap in the disk opens up. When the gap opening occurs, the motion of the sBH is locked to the viscous evolution of the disk, hence, the type-II migration torque is (e.g., Lin & Papaloizou 1986; Ward 1997; Syer & Clarke 1995)

$$J_{\text{mig,II}} = -\frac{2\pi r^2 \Sigma}{m_{\text{sBH}}} r \Omega |v_{\text{gas},r}|, \quad (17)$$

where $v_{\text{gas},r} = -\dot{M}_\bullet/(2\pi r \Sigma)$ is the gas inflow velocity.

Head wind—For a sBH embedded in the gas disk, surrounding gas in its gravitational influence sphere flows towards it. Considering the differential rotation of the disk, the inflow gas generally

carries nonzero angular momentum relative to the sBH. Therefore the inflow tends to form a certain local disk or bulge profile around the sBH. Radiative feedback and magnetic effects drive a major part of the captured material to escape in the form of outflow, therefore only the remaining part is accreted by the sBH (Yang et al. 2014; McKinney et al. 2014). These accreted materials from the headwind can transfer angular momentum to the orbital motion of the sBH, hence exerting a specific torque given by:

$$\dot{J}_{\text{wind}} = -\frac{r\delta v_{\phi}\dot{m}_{\text{gas}}}{m_{\text{sBH}}}, \quad (18)$$

where $\delta v_{\phi} = v_{\phi,\text{gas}} - v_{\phi,\text{sBH}}$ is the head wind speed and \dot{m}_{gas} is gas capture rate (see Pan & Yang 2021a, for detailed calculation).

In a word, the sBH migration timescale in the AGN disk and the nuclear star cluster are (see also, Pan & Yang 2021a)

$$\tau_{\text{mig}}^{\text{d}} = \frac{J}{|\dot{J}_{\text{mig,I/II}} + \dot{J}_{\text{wind}} + \dot{J}_{\text{gw}}|}, \quad \tau_{\text{mig}}^{\text{c}} = \frac{J}{|\dot{J}_{\text{mig,I}} + \dot{J}_{\text{gw}}|}, \quad (19)$$

where the specific torque by GW emissions \dot{J}_{gw} is given by

$$\dot{J}_{\text{gw}} = -\frac{32}{5c^5} \frac{m_{\text{sBH}}}{M} \left(\frac{GM}{r}\right)^{7/2}. \quad (20)$$

When a gap is opened, we set the headwind torque $\dot{J}_{\text{wind}} = 0$.

The evolution of those stars/sBHs with the orbit plane parallel to the accretion disk will be significantly different from the rest. Here we use the following ansatz to study the distribution function evolution of these stars/sBHs on the disk.

3.3 Active stage evolution

To distinguish those stars/sBHs on the disk plane, we name these stars/sBHs as "disk stars/sBHs" in the following and denote their distribution function as $g_{s/\text{sBH}}(t, E, \mathcal{R}, m)$, while we still use $f_{s/\text{sBH}}$ to describe the distribution of the star/sBHs with orbits out of the disk plane (in the following these stars/sBHs will be named as "cluster stars/sBHs"). Before we write down the evolution equations for the cluster/disk stars/sBHs distributions, several important points need to be noticed:

(1) The orbit of the disk stars/sBHs will be quickly circularized due to their interaction with the accretion disk (see Eq.(16)). This indicates that we can make the approximation $\mathcal{R} \approx 1$ in the $g_{s/\text{sBH}}(t, E, \mathcal{R}, m)$, and therefore we reduce the \mathcal{R} -direction in the phase space and define:

$$g_{s/\text{sBH}}(t, E, m) = \int_0^1 g_{s/\text{sBH}}(t, E, \mathcal{R}, m) d\mathcal{R}. \quad (21)$$

Moreover, the advection term D_E in the E -direction overwhelms the diffusion term D_{EE} for the disk stars/sBHs because the star-disk interaction mainly affects the advection term. Therefore, we can approximate $D_{EE} = 0$ in the evolution equation of $g_{s/\text{sBH}}(t, E, m)$.

(2) The exchange of stars/sBHs between the nuclear star cluster and the disk involves two processes: the capture of the cluster stars/sBHs by the disk through the damping of the orbital inclination angle, and the scattering of the stars/sBHs from the disk to the cluster. The timescale of these two processes is much shorter than the migration timescale, especially for orbiters with small inclination angles. Therefore, a local equilibrium can be approximately established, which leads to the phenomenological source term in the Fokker-Planck equation given as $S_{s/\text{sBH}} = \mu_{s/\text{sBH}} f_{s/\text{sBH}} / \tau_{\text{mig}}^{\text{d}}$ (see also, Vilkovskij & Czerny 2002; Kennedy et al. 2016; Panamarev et al. 2018; Pan & Yang 2021a), where the $f_{s/\text{sBH}}$ is the stars/sBHs distribution function in the nuclear star cluster. The net

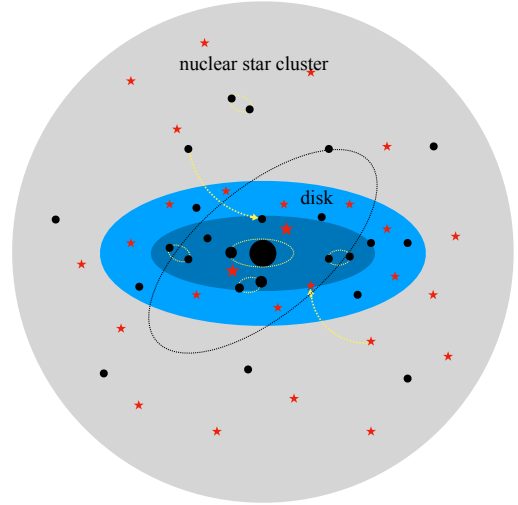


Figure 1. Schematic picture of the physical scenario in our work. A MBH is located at the galaxy centre, with a surrounding accretion disk and a population of stars/sBHs. The disk can capture the stars/sBHs from the nuclear star cluster and increase the EMRI rate by the star/sBH-disk interaction. For stars/sBHs embedded in the disk, they will grow by accreting the disk gas. Meanwhile, under the influence of the sBH-disk interaction, sBHs in the disk will can form binaries and merge, which contributes to the gravitational wave sources. In the main text, the Fokker-Planck equation is adopted to describe the evolution of the mass distribution function for sBHs and stars.

capture rate will be determined by parameter $\mu_{s/\text{sBH}}$. Here, we set $\mu_{\text{sBH}} = \mu_s m_{\text{sBH}} / m_s$, and μ_s is an adjustable parameter (see also Pan & Yang 2021a). It is clear to see that the larger cluster population $f_{s/\text{sBH}}$ and stronger migration (shorter $\tau_{\text{mig}}^{\text{d}}$) means a larger capture effect.

(3) As mentioned in the previous section, the collapse of the massive stars to the sBHs is a complicated process that depends on many physical factors, this process is phenomenologically treated with a lifetime T_s of stars in disk. Note that we assume a homogeneous mass distribution of the stars ($m_s = M_{\odot}$) in the nuclear star cluster where the accretion is absent, therefore $f_s(m_s, E)$ in the equation (22) can be written as $f_s(m_s, E) = f_s(E)\delta(m_s - M_{\odot})$.

Now we are ready to write down the evolution equations in the active stage:

$$\begin{aligned} \mathcal{C} \frac{\partial f_{\text{sBH}}}{\partial t} &= -\frac{\partial F_E^{\text{sBH}}}{\partial E} - \frac{\partial F_{\mathcal{R}}^{\text{sBH}}}{\partial \mathcal{R}} - \mathcal{C} \mu_{\text{sBH}} \frac{f_{\text{sBH}}}{\tau_{\text{mig}}^{\text{d,sBH}}}, \\ \mathcal{C} \frac{\partial f_s}{\partial t} &= -\frac{\partial}{\partial E} F_E^s - \frac{\partial}{\partial \mathcal{R}} F_{\mathcal{R}}^s - \mathcal{C} \mu_s \frac{f_s}{\tau_{\text{mig}}^{\text{d,s}}}, \\ \frac{\partial g_{\text{sBH}}}{\partial t} &\approx \frac{1}{\mathcal{C}} \frac{\partial (D_E^{\text{d,sBH}} g_{\text{sBH}})}{\partial E} - \frac{\partial (g_{\text{sBH}} \dot{m}_{\text{sBH}})}{\partial m} + \\ &\quad \frac{g_s(\epsilon m_{\text{sBH}})}{T_s} + \mu_{\text{sBH}} \frac{\bar{f}_{\text{sBH}}}{\tau_{\text{mig}}^{\text{d,sBH}}}, \\ \frac{\partial g_s}{\partial t} &\approx \frac{1}{\mathcal{C}} \frac{\partial (D_E^{\text{d,s}} g_s)}{\partial E} - \frac{\partial (g_s \dot{m}_s)}{\partial m} - \frac{g_s(m_s)}{T_s} + \mu_s \frac{\bar{f}_s}{\tau_{\text{mig}}^{\text{d,s}}}, \end{aligned} \quad (22)$$

where $\bar{f}_s = \int_0^1 d\mathcal{R} f_s$, $\bar{f}_{\text{sBH}} = \int_0^1 d\mathcal{R} f_{\text{sBH}}$ and T_s is the lifetime of stars in disk. In addition, $F_E, F_{\mathcal{R}}$ is defined in equation (3), with the

advection coefficients modified as

$$D_E^{i,j} \rightarrow D_E^j - \mathcal{C} \frac{E}{\tau_{\text{mig}}^{i,j}},$$

$$D_{\mathcal{R}}^{i,c} \rightarrow D_{\mathcal{R}}^j - \mathcal{C} \frac{1 - \mathcal{R}}{\tau_{\text{mig}}^{c,j}},$$
(23)

where $i = \{c, d\}$ and $j = \{\text{star}, \text{sBH}\}$. The superscript "c" and "d" mean "cluster" and "disk", respectively. Note that we set $\varepsilon = 10$ since roughly 90% of the mass of the progenitor star for $50M_{\odot} < m_s < 150M_{\odot}$ will be lost during the supernova explosion (see [Nomoto et al. 2013](#)). We also assume the lifetime T_s of stars with mass in range of $[50M_{\odot}, 150M_{\odot}]$ is 5 Myr (e.g., [Toyouchi et al. 2022](#)). For stars with $m_s > 150M_{\odot}$, they undergo thermonuclear explosions triggered by pair-creation instability. Such stars are completely disrupted without forming a sBH (e.g., [Umeda & Nomoto 2002](#); [Heger & Woosley 2002](#); [Nomoto et al. 2013](#)). We don't consider the gravitational collapse of the stars with mass $m_s < 50M_{\odot}$ since their lifetime is much longer than 5 Myr.

The initial condition for solving the above distribution evolution is the results of the 5 Gyr spherically symmetric evolution when the disk is absent. If we assume that the solid angle spanned by the disk is around 1%, then the initial distribution function for cluster stars/sBHs is given by $f_{s/\text{sBH}}(t_{\text{ini}}^{\text{active}}) = 99\% \times f_{s/\text{sBH}}(t_{\text{end}}^{\text{quiet}})$, while $g_{s/\text{sBH}}(t_{\text{ini}}^{\text{active}}, E, m_{s/\text{sBH}}) = 1\% \times \int d\mathcal{R} f_{s/\text{sBH}}(t_{\text{end}}^{\text{quiet}})$ for disk stars/sBHs, which is similar to the settings in [Pan et al. \(2022\)](#).

The boundary conditions for the distribution of the cluster stars/sBHs are the same as the quiet stage at the boundary of $E = 0$ and $\mathcal{R} = 1$. At the loss cone boundary in the active stage, it can be set $F_R = 0$ since the fast eccentricity damping by density waves drives stars/sBHs away from the loss cone (see also [Pan & Yang 2021a](#)). For the disk stars/sBHs, only two boundary conditions are required, which is

$$g_i(t, E)|_{E \rightarrow 0} = g_i(t = 0, E)|_{E \rightarrow 0},$$

$$\left. \frac{\partial [\dot{m}_i g_i(t, E, m_i)]}{\partial m_i} \right|_{m_i = m_{i,\text{min}}} = \frac{\dot{m}_i g_i(t, E, m_{i,\text{min}})}{\Delta m_i},$$
(24)

where $m_{i,\text{min}}$ is the minimum mass of sBH/star, Δm_i is the mass grid in log-scale and $i = \{\text{star}, \text{sBH}\}$. For the sBHs, the \dot{m}_{sBH} takes the value of $1\dot{M}_{\text{Edd}}$ in the outer disk region and $2 - 50\dot{M}_{\text{Edd}}$ in the inner disk region. For the stars, we set the \dot{m}_s takes the value of $1\dot{M}_{\text{Edd}}$ in the outer disk region and follows equation (5) in the inner disk region. The first boundary condition comes from the approximation that the migration rate when $E \rightarrow 0$ is very low.

4 SIMULATION RESULTS

Following the above procedure, we consider a model consisting of stars/sBHs orbiting around a MBH ($M_{\bullet} \in [10^5, 10^{10}]M_{\odot}$), where part of the stars/sBHs embedded in the accretion disk while others still stay in spherical star cluster. We set the initial condition to be the stars with a monochromatic mass distribution at $m_s = 1M_{\odot}$ and the sBHs with masses of $m_{\text{sBH}} \in [5, 15]M_{\odot}$ if they stay in spherical star cluster (see [Nomoto et al. 2013](#), for a review). It should be noted that, in the simulation of the Fokker-Planck equation, the loss rate enhancement of stars using the complete mass distribution function compared to that of using the monochromatic mass function is in the range of 1 - 2 (see [Magorrian & Tremaine 1999](#); [Kennedy et al. 2016](#)). Thus, for numerical simplicity, we adopt a monochromatic mass function for cluster stars, which will not affect our main conclusion (see also, [Cohn & Kulsrud 1978](#); [Amaro-Seoane & Preto](#)

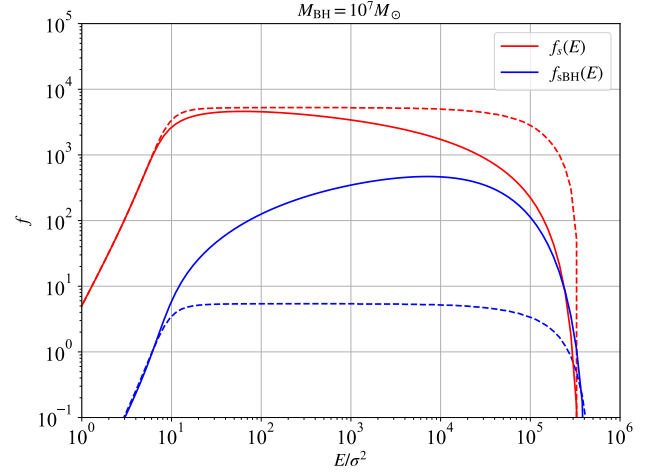


Figure 2. Evolution of stars and sBHs during the quiet stage. We plot the marginal distribution function $f_{s/\text{sBH}}(E) = \int dm d\mathcal{R} f_{s/\text{sBH}}(E, \mathcal{R}, m)$ of the stars and sBHs in the unit of $\text{pc}^{-3} \sigma_{*}^{-3}$. The blue/red dashed and solid lines represent the initial marginal sBH/star distribution and that after 5 Gyrs evolution, respectively. The mass of the central MBH is set to be $10^7 M_{\odot}$ in plotting this figure.

[2011](#); [Stone et al. 2017](#); [Pan & Yang 2021a](#); [Broggi et al. 2022](#)). The accretion effect will be considered if we introduce the accretion disk in the active stage of a galaxy, where the mass growth is determined by the accretion rate and the accretion time. We assume that the total relative abundance of sBH $\varphi = 0.001$ and the density power-law index of $\gamma = 1.5$ ([Tremaine et al. 1994](#); [Binney & Tremaine 2008](#)). The influence radius within which the central MBH dominates the gravitational field is defined from the velocity dispersion of the spheroid of the galaxy, which follows the $M_{\bullet} - \sigma_{*}$ relation in equation (7).

4.1 Quiet stage

During the quiet stage, the evolution of the distribution function follows the standard way, in which we choose the mass distribution as $dN_s/dm_s \propto \delta(m_s - M_{\odot})$ for stars and $dN_{\text{sBH}}/dm_{\text{sBH}} \propto m_{\text{sBH}}^{-2.35}$ within $m_{\text{sBH}} \in [5, 15]M_{\odot}$ for sBHs. The evolution time is set to be 5 Gyr for the quiet stage. The evolution of the marginal distribution function $f_{s/\text{sBH}}(E) = \int dm d\mathcal{R} f_{s/\text{sBH}}(E, \mathcal{R}, m)$ is plotted in Fig. 2, while the $f_{s/\text{sBH}}(m) = \int dE d\mathcal{R} f_{s/\text{sBH}}(E, \mathcal{R}, m)$ is almost unchanged since there is no mass accretion effect during the quiet stage. In Fig. 2, the density profile of the more massive sBH component for $r < r_h$ is steeper than that of the star component. This is because of the mass segregation effect ([Amaro-Seoane & Preto 2011](#); [Amaro-Seoane 2018](#)) which we briefly describe as follows. The total number of stars/sBHs will decrease since they fall into the MBH via the loss cone mechanism. Only in the inner region ($r < r_h$, where $r_h \equiv GM_{\bullet}/\sigma_{*}^2$ is the influence radius of MBH), the number of stars decreases while the number of sBHs increases. In the inner region, the increase of the sBHs' population is due to the inward migration of the sBHs from the outer region. In the simulation using the Fokker-Planck equation, the heavier sBHs migrate inward faster than the stars, which is known as the mass segregation effect. Thus, the density profile of the more massive sBH component is steeper than that of the star component due to the mass segregation effect.

The results of the quiet stage will be the initial condition for the active stage.

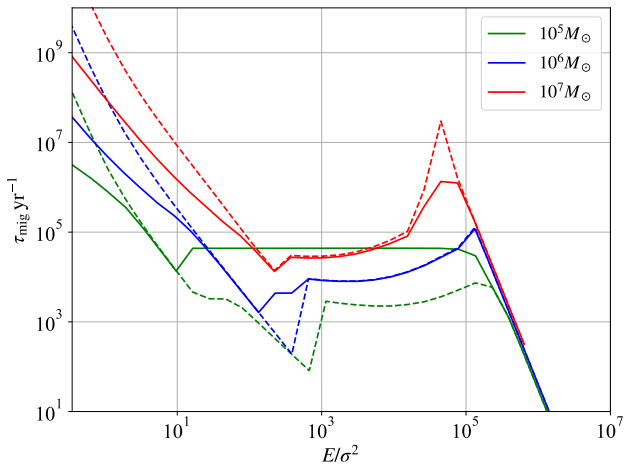


Figure 3. Migration time scale $\tau_{\text{mig}}(E/\sigma_*^2)$. The dashed lines are the migration time scale for the stars/sBHs on the disk with different central BH masses, while the solid lines are the migration time scale for the stars/sBHs in the nuclear star cluster. The mass of the star and sBH here is chosen to be $10M_\odot$ as fiducial.

4.2 Active stage

For the galaxy entering the active stage, an SG-disk with accretion rate $\dot{M}_\bullet = 0.1\dot{M}_{\text{Edd}}$ and $\alpha = 0.1$ are assumed, the accretion disk will affect both the dynamics of the stars/sBHs and the mass distributions. The features of the evolution during the active stage can be summarised as follows.

The radius/energy-dependent migration timescale shown in Fig. 3 has a key effect on the evolution of the distribution functions. The migration rate τ_{mig} of the cluster stars/sBHs in the outer region ($E/\sigma_*^2 < 10$) is significantly lower than that in the inner region of the galaxy centre ($E/\sigma_*^2 > 10^4$). This means that the distribution of the stars/sBHs will not deviate significantly from the initial distribution function in the outer region, while the distribution changes significantly in the inner region due to the strong migration effect. The migration timescale become much shorter at $E/\sigma_*^2 \sim 10^3$ (see Fig. 3), which also means a higher capture rate (for a fixed μ) since it is proportional to $\mu/\tau_{\text{mig}}^{\text{d}}$. As shown in Fig. 4(a), we take distribution function of $m_{\text{sBH}} = 10M_\odot$ with $\mu_s = 0.1$ and $M_\bullet = 10^7 M_\odot$ as an example. The stars/sBHs distribution functions in the cluster will have a dip within the energy range $10 < E/\sigma_*^2 < 10^4$ due to the capture by the disk, while a peak structure around $10^4 < E/\sigma_*^2 < 10^5$ is due to the traffic effect induced by the longer migration timescale. The distribution function of sBH in the cluster decreases with time evolution due to the capture by disk, which means that the cluster will provide fewer and fewer sBHs. Moreover, since the migration and capture rate is proportional to the sBH mass, the heavier sBH will have a stronger migration rate and a stronger capture rate, leading to a steeper distribution function at higher energy and a shallower distribution function at fast capture region (see Fig. 4(b)).

In Fig. 4(c), we show the distribution function of $m_{\text{sBH}} = 10M_\odot$ and $20M_\odot$ in the disk during different evolution stages. The peaks of these distribution functions gradually shift to the high energy region until it reaches local equilibrium, i.e., the capture rate from the cluster is equal to the inward migration rate. The peak of the distribution function around $E/\sigma_*^2 \approx 5 \times 10^4$ in the equilibrium state is due to the traffic effect and it is consistent with the peak in the figure

of migration timescale Fig. 3. Due to the accretion, the distribution function of lighter sBHs gradually decreases while the distribution function of heavier sBHs gradually increases. It is worth mentioning that, evolving to the equilibrium stage, the total number of sBHs in the disk decreases with time since some of them plunge into the centre MBH and the capture rate from the cluster also decreases with time. In this way, the wet EMRI rate will also decay over time, which is consistent with the result in Pan et al. (2022). Similarly, the distribution function of stars with $m_s = 50M_\odot$ and $150M_\odot$ is shown in Fig. 4(d). In the unstable region of disk, the stars can not grow to $50M_\odot$ due to their low accretion rate ($\dot{m}_s = \dot{M}_{\text{Edd}}$). In the stable region of disk, only the stars around the peak of migration timescale $E/\sigma_*^2 \approx 5 \times 10^4$ have enough time to become so massive.

The above information on the evolution of distribution functions of the stars/sBHs could be useful to understand the black hole distribution in the AGN disk and also the gravitational waves emitted from the corresponding EMRI events, as we shall discuss in the next sections.

5 MASS DISTRIBUTION OF SBHS IN DISK

Up to now, more than 90 stellar-mass BBH merging events have been detected by Advanced LIGO (LIGO Scientific Collaboration et al. 2015) and Advanced Virgo (Acernese et al. 2015). However, the origin of these sBH binaries is still unclear. The accretion disk provides a unique environment for BBHs to merge (see Mandel & Farmer 2022, for a review). In such a gas-rich environment, the disk-binary interaction will accelerate the binary merge (e.g., Gröbner et al. 2020). In addition, the migrating object will be trapped in the location where $\dot{J}_{\text{mig},\text{I}}$ changes its sign from negative to positive in the decreasing r direction, which is called migration trap (e.g., Lyra et al. 2010; McKernan et al. 2012, 2014; Bellovary et al. 2016; Secunda et al. 2019). These migration traps are favorable places for BBH formation (e.g., Secunda et al. 2019; Peng & Chen 2021). Various works (e.g., Stone et al. 2017; Yang et al. 2019b,a; Gröbner et al. 2020; Gerosa & Fishbach 2021) suggested that the AGN-assisted BBH merger rate is about $(0.02 - 60)\text{Gpc}^{-3}\text{yr}^{-1}$, which could be responsible for 10% – 50% of gravitational-wave detections. Meanwhile, of the BBH mergers that have been detected, many sBHs are bigger than $30M_\odot$, which are much larger than the remnants of traditional stellar evolution ($\sim 10M_\odot$). These massive sBHs are usually regarded as the remnants of the hierarchical sBH mergers (see Kohler 2017; Yang et al. 2019a). Here, we expect that accretion could offer another channel to form massive sBHs detected by LIGO/Virgo.

Moreover, future upgraded ground-based GW detectors will detect a large amount of binary sBH merger events. A sub-species of these binary merger events may have EM counterparts if they happen in the AGN disk. It should be noted that it is difficult to find out this kind of EM counterpart due to the bright background emission from the AGN disk. Up to now, ten possible candidate EM counterparts to BBH mergers are reported in Graham et al. (2020, 2022). Therefore it is worth investigating the effect of the accretion of the sBH in the disk on the mass distribution of these BBH merger events. On the other hand, multi-messenger observations in the future on these sources will be beneficial to the understanding of the galaxy centre environment.

In Fig. 5(a), we show a typical mass distribution during the active stage where the accretion rate $\dot{m}_{\text{sBH}} = 20\dot{M}_{\text{Edd}}$ in the inner region of disk and $\dot{m}_{\text{sBH}} = \dot{M}_{\text{Edd}}$ in the outer region. The peak gradually shifts to the more massive region over time due to mass growth by accre-

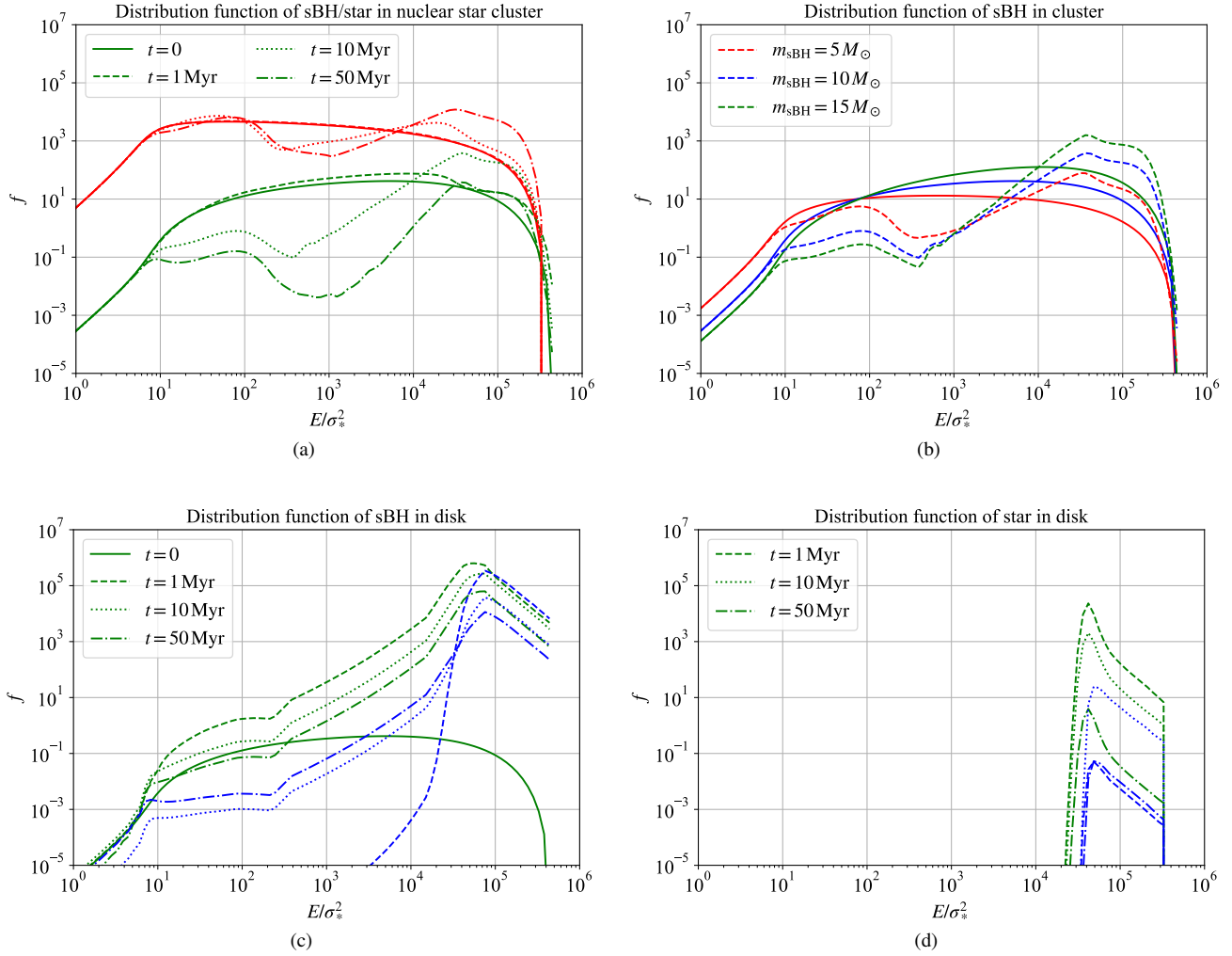


Figure 4. The evolution of the distribution function of the stars/sBHs. *Left upper panel:* the evolution of the distribution function for stars/sBHs in nuclear star cluster. The red and green lines represent the distribution function $f_s(t, E) = \int f_s(t, E, m_s) \delta(m_s - M_\odot) dm_s$ in unit of $\text{pc}^{-3} \sigma_*^{-3}$ for stars and $f_{\text{sBH}}(t, E, m_{\text{sBH}} = 10 M_\odot)$ in the unit of $\text{pc}^{-3} \sigma_*^{-3} M_\odot^{-1}$ for sBHs, respectively. *Right upper panel:* the evolution of the sBH's distribution function in nuclear star cluster at $t = 10 \text{ Myr}$ for different masses of sBHs, where the solid and dashed lines represent the initial distribution and that at $t = 10 \text{ Myr}$ in the unit of $\text{pc}^{-3} \sigma_*^{-3} M_\odot^{-1}$, respectively. *Left lower panel:* the evolution of the sBH's distribution function in AGN disk, where the green and blue lines represent the distribution $f_{\text{sBH}}(t, E, m_{\text{sBH}})$ in the unit of $\text{pc}^{-3} \sigma_*^{-3} M_\odot^{-1}$ with $m_{\text{sBH}} = 10 M_\odot$ and $m_{\text{sBH}} = 20 M_\odot$, respectively. *Right lower panel:* the evolution of the star's distribution function in AGN disk, where the green and blue lines represent the distribution $f_{\text{sBH}}(t, m_s)$ in a unit of $\text{pc}^{-3} \sigma_*^{-3} M_\odot^{-1}$ with $m_s = 50 M_\odot$ and $m_s = 150 M_\odot$, respectively.

tion. Some sBHs can even grow up to $100 M_\odot$, which is determined by their accretion rate and the duration of the migration process in the disk.

Detection of a BBH merger event can be understood as sampling over many host galaxies with different parameters, such as the evolution stage of the galaxy, the galaxy's centre MBH mass, disk lifetime (duty cycle) T_{disk} , etc. To obtain the number density distribution dn/dm_{sBH} of sBH in the AGN disk relevant to the future GW detection, we need to average our number density of the sBH over the centre MBH mass $M_\bullet \in [10^5 - 10^{10}] M_\odot$, evolution time $t \in [0, T_{\text{disk}}]$ and the disk lifetime $T_{\text{disk}} \in [T_{\text{disk}}^{\text{min}}, T_{\text{disk}}^{\text{max}}]$. Firstly, we can compute the number density per unit sBH mass with a fixed duty cycle defined as:

$$\frac{dn}{dm_{\text{sBH}}} = \int_0^{T_{\text{disk}}} \frac{dt}{T_{\text{disk}}} \int_{10^5 M_\odot}^{10^{10} M_\odot} d \log M_\bullet \frac{dN(M_\bullet, t)}{dm_{\text{sBH}}} \phi_{\text{bh}} f_{\text{wet}}, \quad (25)$$

where ϕ_{bh} is the local MBH mass function (see Figure 5 in [Barausse](#)

[2012](#)) and the fraction of AGN f_{wet} is assumed as 1%. Furthermore, we can estimate the distribution of BBH mergers over mass in AGN disk as ([Gröbner et al. 2020](#))

$$\frac{dR}{dm_{\text{sBH}}} = \frac{dn}{dm_{\text{sBH}}} \frac{f_b}{\tau_{\text{med}}}, \quad (26)$$

where we set $f_b = 0.1$ as a typical fraction of such sBHs residing in the binaries ($f_b \sim 0.01 - 0.2$ in [McKernan et al. 2018](#)) and $\tau_{\text{med}} = 7 \times 10^6 \text{ yr}$ as a typical median BBHs merger timescale in the disk ($\tau_{\text{med}} \sim 10^6 - 10^8 \text{ yr}$, which depends on disk parameters and sBH binaries' initial orbital parameters, see [Gröbner et al. 2020](#)). We show the results in red solid, blue dashed, green dotted and orange dash-dotted lines for $T_{\text{disk}} = \{5, 10, 50, 100\} \text{ Myr}$ in Fig. 5(b). Moreover, we show the ensemble average in black solid line over the AGN disk lifetime T_{disk} , i.e.,

$$\frac{d\bar{R}}{dm_{\text{sBH}}} = \frac{1}{T_{\text{disk}}^{\text{max}} - T_{\text{disk}}^{\text{min}}} \int_{T_{\text{disk}}^{\text{min}}}^{T_{\text{disk}}^{\text{max}}} dT_{\text{disk}} \frac{dR}{dm_{\text{sBH}}}, \quad (27)$$

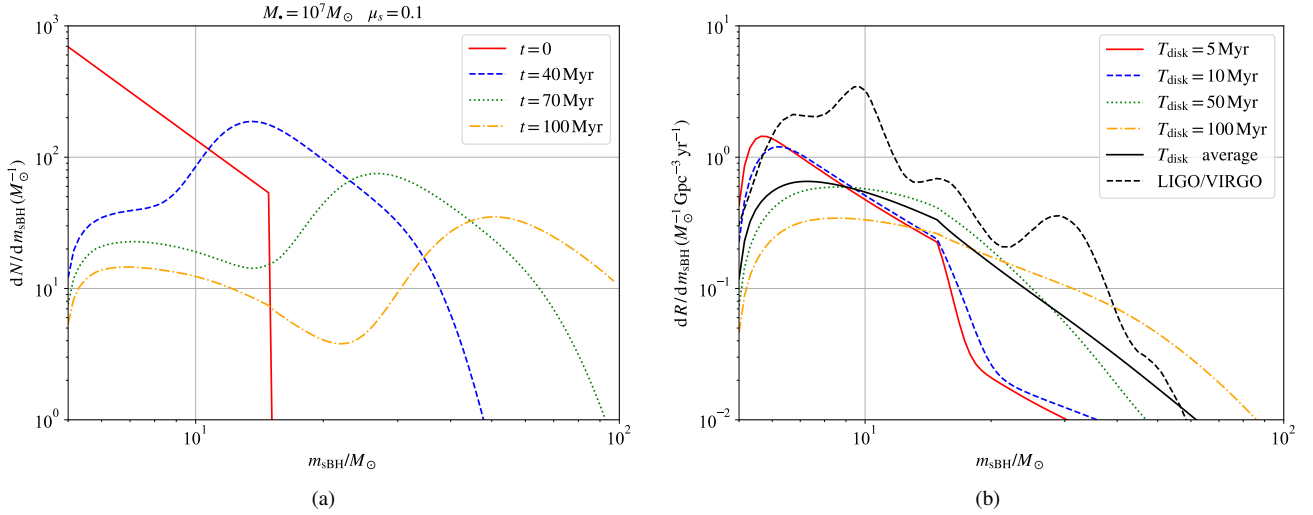


Figure 5. The mass distribution of sBH in the disk. *Left panel:* an example of the mass-distribution evolution for different timescales for a MBH with $M_{\bullet} = 10^7 M_{\odot}$ and capture rate $\mu_s = 0.1$, where $\dot{M} = \dot{M}_{\text{Edd}}$ and $\dot{M} = 20\dot{M}_{\text{Edd}}$ are adopted for sBHs in the outer gravitationally unstable region and inner standard disk region, respectively. *Right panel:* the number density distribution of sBH binary merger event. The black solid line represents the average distribution over different disk lifetimes within $T_{\text{disk}} \in [1, 100]$ Myr. For comparison, the black dashed line represents the mass distribution reconstructed from the merging BBHs as observed by LIGO/Virgo.

where $T_{\text{disk}}^{\text{min}} = 1$ Myr and $T_{\text{disk}}^{\text{max}} = 100$ Myr (e.g., Shulevski et al. 2015; Turner 2018). For comparison, we also show the BBH merger event distribution over mass reconstructed from the merging BBHs observed by LIGO/Virgo (Tiwari & Fairhurst 2021) in the black dashed line. Our results show that the AGN-assisted BBH merger rate in the disk could be responsible for 10% – 30% of gravitational-wave detections. The peak of binary sBH mass distribution observed by the ground based gravitational wave detector is at about $9 M_{\odot}$ (see Tiwari & Fairhurst 2021; van Son et al. 2022). The accretion effect of sBHs in the disk in our model could be one possible reason that contributes to the dearth of low-mass binary sBH by shifting the sBHs population to the more massive region.

6 EMRI EVENT RATE

The above simulation results of the distribution function evolution can be used to study the influence of the accretion on the EMRI event rate, which will be related to the stochastic GWB contributed by EMRI events in the next section. Following the definition in Pan et al. (2021), we name EMRIs in quiet/active stage as dry/wet EMRIs with event rates denoted as $\Gamma_{\text{dry/wet}}$, respectively. For the dry EMRI per MBH with sBH mass m_{sBH} , the EMRI rate via loss cone mechanism is given by (e.g., Hopman & Alexander 2005; Amaro-Seoane & Preto 2011; Pan & Yang 2021a)

$$\Gamma_{\text{dry}}(m_{\text{sBH}}) = \int_{E > E_{\text{gw}}} \vec{F} \cdot d\vec{l} \quad (28)$$

where $E_{\text{gw}} = GM_{\bullet}/2r_{\text{gw}}$ with $r_{\text{gw}} = 0.01r_h$, $\vec{F} = \{F_E, F_R\}$ is the flux of star/sBH along the line element of the loss cone boundary $d\vec{l} = \{dE, dR\}$. It is important to note that the real observation is over an ensemble of EMRI sources with different evolution times. Therefore we need to have a time/ensemble averaged event rate, hence the total mean EMRI rate overall sBH masses averaged within time T is defined as:

$$\bar{\Gamma} = \int dm_{\text{sBH}} \int_0^T \frac{dt}{T} \Gamma(m_{\text{sBH}}, t). \quad (29)$$

For simplicity, we take the fitting formula obtained by Broggi et al. (2022) for the mean dry EMRI rate, where they assumed $m_{\text{sBH}} = 10 M_{\odot}$ and suggested that the best-fit to the mean dry EMRI rate within a Hubble time $T_H \sim 10$ Gyr:

$$\bar{\Gamma}_{\text{dry}} = 130 \left(\frac{M_{\bullet}}{4 \times 10^6 M_{\odot}} \right)^{1.03} \text{Gyr}^{-1}. \quad (30)$$

Note that the dry EMRI rate reproduced in our calculation shows that the above $\bar{\Gamma}_{\text{dry}}$ is only slightly affected by extending the monochromatic distribution ($m_{\text{sBH}} = 10 M_{\odot}$) to the power-law distribution ($dN/dm_{\text{sBH}} \propto m_{\text{sBH}}^{-2.35}$ with $5 M_{\odot} < m_{\text{sBH}} < 15 M_{\odot}$). Therefore, we make use of the above equation for the dry EMRI rate in our work. In the active stage of the galaxy, the wet EMRI rate is proportional to the distribution function/number density of sBHs around the E_{max} boundary. Furthermore, the sBHs' number density of the disk component is several orders of magnitude higher than that of the cluster component at E_{max} boundary (see Fig. 4(a) and Fig. 4(c)). In this case, the wet EMRI rate will be dominated by the sBHs in the disk, which can be given by

$$\Gamma_{\text{wet}}(m_{\text{sBH}}) = -\mathcal{E} D_E^d g_{\text{sBH}} \Big|_{E=E_{\text{max}}}. \quad (31)$$

It should be noted that the wet EMRI rate is determined by the E -direction flux at the E_{max} boundary while R -direction flux is no longer important due to the strong orbit circularisation in the active stage. To obtain the averaged wet EMRI rate via equation (29), the time average should be over the disk lifetime thereby $T = T_{\text{disk}}$.

We show the time dependence total wet EMRI rate $\bar{\Gamma}_{\text{wet}} = \int \bar{\Gamma}_{\text{wet}}(m_{\text{sBH}}) dm_{\text{sBH}}$ for $\mu_s = \{0.01, 0.1\}$ with different sBH accretion rates in Fig. 6. For a fixed μ_s/m_{sBH} , the accretion has a slight promotion on the EMRI rate at the early and middle stages of the evolution. This is because the accretion increases the mass of the sBH, thereby increasing the migration rate. Meanwhile, during the duty cycle of disk, there are about 70 sBHs formed by collapsing stars, which can also increase less than 10% of the EMRI rate. After reaching a peak, the event rate will gradually decrease since more and more sBHs plunged into the MBH. The capture rate has little effect

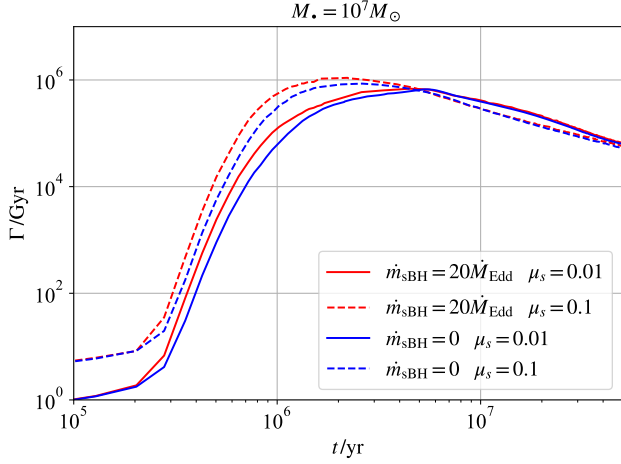


Figure 6. The time dependence of wet EMRI rate. The solid and dashed lines represent the capture rate of $\mu_s = 0.01$ and $\mu_s = 0.1$ respectively. The blue and red lines show the accretion rate of $\dot{m}_{\text{sBH}} = 0$ and $\dot{m}_{\text{sBH}} = 20\dot{M}_{\text{Edd}}$, respectively.

on a long-time averaged (mean) EMRI rate ($\bar{\Gamma}_{\text{wet}}$ with $t > 10\text{Myr}$) since the total number of sBHs is the same at different capture rates, capture rate only affects how the Γ evolves with time. However, the mass accretion of sBH can affect the mass distribution of sBH in the EMRI system. In Fig. 7, we show how the total mean wet EMRI rate $\bar{\Gamma}_{\text{wet}}$ within $m_{\text{sBH}}^i < m_{\text{sBH}} < m_{\text{sBH}}^{i+1}$ depends on the accretion rate of the sBH for two systems with different MBH masses. Since for low-mass AGN, the migration time of sBH is comparatively short, the accretion effect on sBH does not have enough time to accumulate and hence has little effect on the wet EMRI rate (see the upper panel of Fig. 7). On the other hand, the accretion effect is not negligible in massive galaxies (see the lower panel of Fig. 7), which will significantly increase the wet EMRI events consisting of heavier sBH and MBH.

In general, the wet EMRI rate is 2-3 orders of magnitude higher than the dry EMRI rate. For a single EMRI source, the dry and wet EMRI events could be distinguishable by observing the GW waveform due to their different eccentricity. The wet EMRI triggered by star-disk interaction tends to be in a circular orbit while the dry EMRI triggered by multi-body scattering tends to be in an elliptical orbit (Babak et al. 2017; Amaro-Seoane 2018; Bonetti & Sesana 2020). The waveform of EMRI in an eccentric orbit will be eccentric GW bursts (e.g., Loutrel 2020a,b), while the EMRI in a circular orbit has an approximate sinusoidal GW waveform.

7 STOCHASTIC GRAVITATIONAL WAVE BACKGROUND IN MILLI-HERTZ BAND

In this section, we present the stochastic gravitational wave background of wet EMRI. The wet EMRI rate will be 2-3 orders of magnitude higher than the dry EMRI due to star-disk interactions, which means a stronger GWB. Moreover, we also include the effect of sBHs' accretion on the GWB. We follow the calculation procedure in Bonetti & Sesana (2020), which is briefly summarised as follows.

The characteristic strain spectrum of the stochastic gravitational wave background generated by the EMRI sources can be expressed

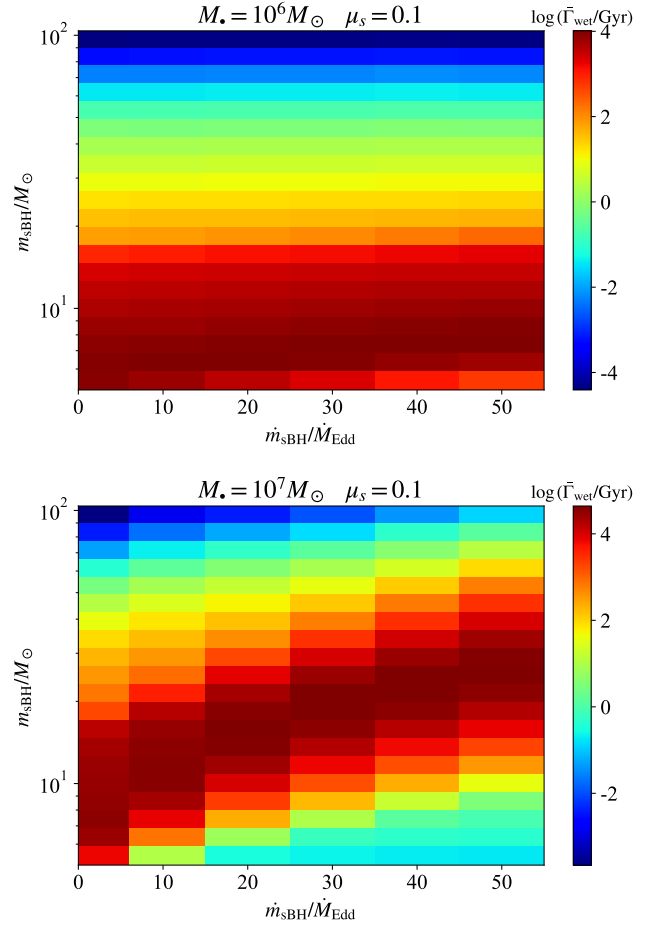


Figure 7. The time-averaged wet EMRI rate within 50Myr for different masses of the sBHs that influenced by different accretion rates $\dot{m}_{\text{sBH}} = \{2, 10, 20, 30, 40, 50\}\dot{M}_{\text{Edd}}$. The color bar is the time-averaged wet EMRI rate $\bar{\Gamma}_{\text{wet}} = \int_{m_{\text{sBH}}^i}^{m_{\text{sBH}}^{i+1}} \bar{\Gamma}_{\text{wet}}(m_{\text{sBH}}) dm_{\text{sBH}}$, where m_{sBH}^i is i -th sBH mass bin of 5 – 100 M_{\odot} in the log-scale. The upper and lower panels represent the cases for $M_{\bullet} = 10^6 M_{\odot}$ and $M_{\bullet} = 10^7 M_{\odot}$ with $\mu_s = 0.1$, respectively.

as (see Bonetti & Sesana 2020, for in detail):

$$h_{\text{c,dry}}^2(f) = \sum_{n=n_{\text{min}}}^{n_{\text{max}}} \int dz d \log M_{\bullet} de_p \begin{cases} \left[n(z, M_{\bullet}, e_p, f_{\text{orb}}) h_n^2(f) \frac{f^2}{\dot{f}} \frac{1}{f T_{\text{obs}}} \right]_{f_{\text{orb}} = \frac{f(1+z)}{n}}, & T_{\text{obs}} > f/\dot{f}, \\ \left[n(z, M_{\bullet}, e_p, f_{\text{orb}}) h_n^2(f) \right]_{f_{\text{orb}} = \frac{f(1+z)}{n}}, & T_{\text{obs}} < f/\dot{f}, \end{cases} \quad (32)$$

where the limits of the harmonic index $n_{\text{min}}, n_{\text{max}}$ are

$$n_{\text{min}} = \frac{f(1+z)}{f_{\text{orb}}(t = T_{\text{obs}})}, \quad n_{\text{max}} = \frac{f(1+z)}{f_{\text{orb}}(t = 0)}, \quad (33)$$

with z the redshift of the galaxy and $f_{\text{orb}}(t)$ is the orbital frequency of the EMRI binary system at time t . The strain of the n -th harmonic component h_n is given by (e.g., Finn & Thorne 2000):

$$h_n^2 = \frac{G\dot{E}_n}{c^3 \pi^2 d^2 f_n^2}. \quad (34)$$

For wet EMRI, the characteristic strain $h_{\text{c,wet}}^2$ has the same form as

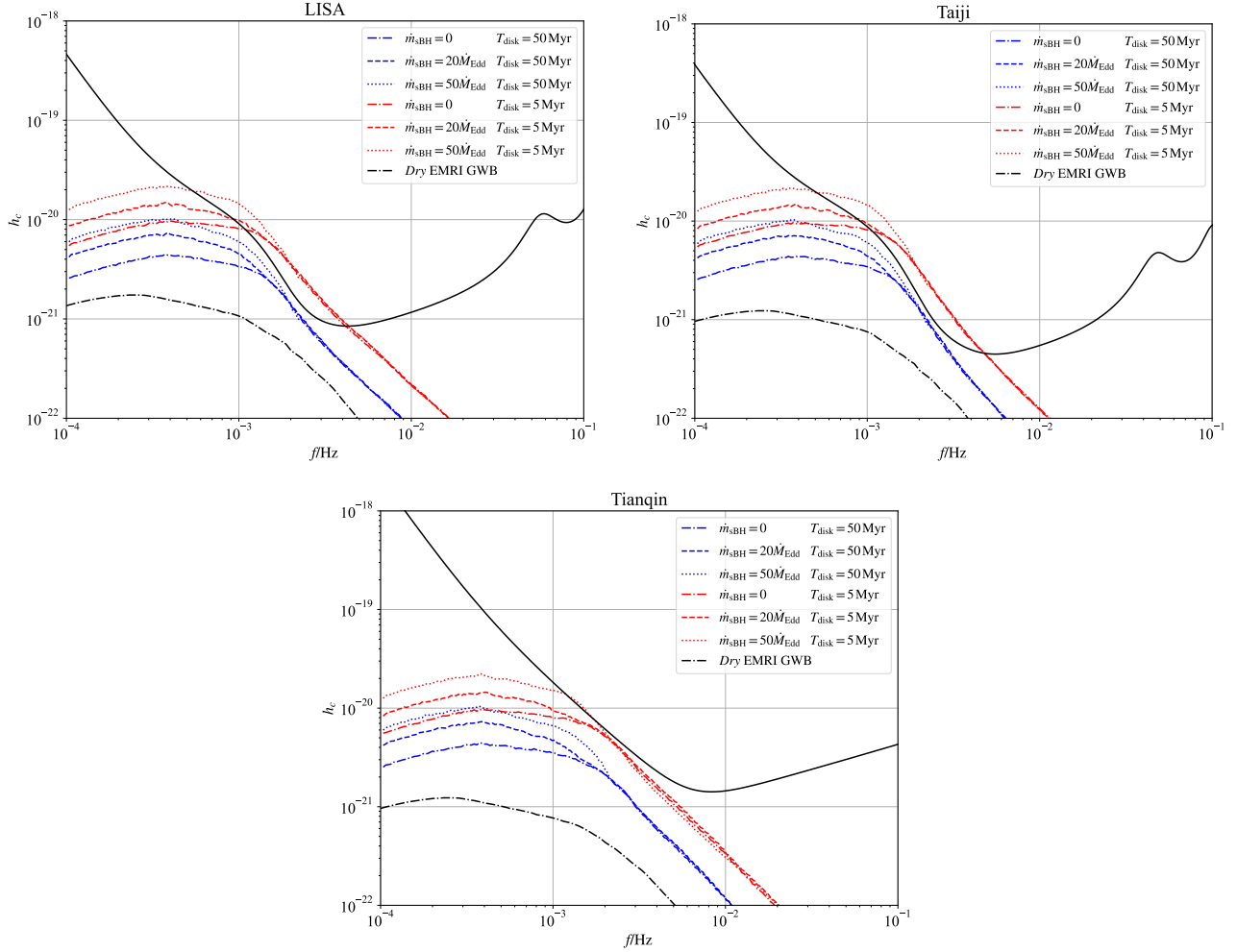


Figure 8. GW background of wet and dry EMRI. The solid black lines are the sensitivity curves of LISA/Taiji/Tianqin. The dash-dotted, dashed and dotted lines show the background with accretion rate $\{0, 20, 50\}\dot{M}_{\text{Edd}}$ for sBHs, respectively, where the disk time of 5 Myr (red) and 50 Myr (blue) are assumed. The black dot-dashed line represents GWB from the dry EMRIs.

the above equation by setting $n = n_{\text{min}} = n_{\text{max}} = 2$, since the EMRI orbit is mostly circularised. The *dry/wet* EMRI rate in the comoving volume of the universe $V_c(z)$ up to redshift z is:

$$n(z, M_\bullet, e_p, f_{\text{orb}}) \equiv \frac{d^4 N_{\text{dry/wet}}}{dz d \log M_\bullet de_p d \ln f_{\text{orb}}} = \frac{d^2 N_{\text{dry/wet}}}{de_p d \ln f_{\text{orb}}} \times \frac{1}{1+z} \frac{dN_\bullet}{d \log M_\bullet} \frac{dV_c(z)}{dz} C_{\text{cusp}}(M_\bullet, z) f_{\text{dry/wet}} \bar{\Gamma}_{\text{dry/wet}}(M_\bullet) T_{\text{obs}}, \quad (35)$$

where the factor $1/(1+z)$ arises from the cosmological redshift, the fraction of AGN f_{wet} is assumed as 1% ($f_{\text{wet}} \sim 1 - 10\%$, see [Martini 2012](#); [Macuga et al. 2019](#)) and $f_{\text{dry}} \equiv 1$, $C_{\text{cusp}}(M_\bullet, z)$ is the fraction of MBHs in the stellar cusps which are supposed to be evacuated during mergers of binary MBHs and regrow afterward ([Babak et al. 2017](#)), and dN_\bullet/dM_\bullet is the redshift-independent MBH mass functions ([Barausse 2012](#)),

$$\frac{dN_\bullet}{d \log M_\bullet} = 0.005 \left(\frac{M_\bullet}{3 \times 10^6 M_\odot} \right)^{-0.3} \text{Mpc}^{-3}. \quad (36)$$

The $\bar{\Gamma}_{\text{dry/wet}}(M_\bullet)$ has been obtained in the previous section.

To calculate the EMRI GWB, we construct a population with $\{M_\bullet, m_{\text{sBH}}, z\}$ following the procedure in [Bonetti & Sesana \(2020\)](#).

For the dry plunge events, the eccentricity at the last stable orbit e_p is sampled from a flat distribution within $e_p \in [0, 0.2]$. For the wet plunge events, we set $e_p = 0$ due to the quick circularisation on the disk plane. Note that not only low SNR (< 20) plunging systems, but also EMRIs in the LISA band which are still tens or even hundreds of years far from the final plunge contribute to the GWBs. Thus, we randomly sample $N_{\text{back}} = \text{int}(T_{\text{back}}/\text{yr})$ points in the range $t \in [0, T_{\text{back}}]$, which represents N_{back} different EMRIs with different starting time t_{ini} . Here the $T_{\text{back}}^{\text{dry}}$ is assumed by ([Bonetti & Sesana 2020](#))

$$T_{\text{back}}^{\text{dry}} = 20 \left(\frac{M_\bullet}{10^4 M_\odot} \right) \text{yr}, \quad (37)$$

For wet EMRIs with the assumption that all orbits are circular, the maximum backward time is set by the observation frequency window of the spaceborne GW detectors. Suppose we set the lower limit of the space-borne detector to be 10^{-4} Hz, then we have $T_{\text{back}}^{\text{wet}} = T_{\text{back}}^{\text{wet}} [2f_{\text{orb}}/(1+z) = 10^{-4} \text{Hz}]$. The next step is we integrate the orbital evolution backward in time for $t_{\text{back}} \sim [0, T_{\text{back}}]$ for each of N_{back} EMRI samples following [Peters \(1964\)](#), i.e.,

$$\{M_\bullet, m_{\text{sBH}}, z, e_p, f_p\} \xrightarrow{t_{\text{back}}} \{M_\bullet, m_{\text{sBH}}, z, e(t=0), f_{\text{orb}}(t=0)\}, \quad (38)$$

Model	$T_{\text{disk}}/\text{Myr}$	$\dot{m}_{\text{sBH}}/\dot{M}_{\text{Edd}}$	(S/N) _{GWB}		
			LISA	Tianqin	Taiji
wet	5	0	1526	183	2790
	5	20	1698	204	3126
	5	50	1879	264	3261
	50	0	236	29	424
	50	20	255	32	456
	50	50	292	43	484
dry	--	--	18	3.7	28

Table 1. SNR of GWB for mission duration $T_{\text{obs}} = 4\text{yr}$. The first column (Wet/Dry) is the EMRI model. The second column is the AGN disk lifetime. The third column is the accretion rate of sBH in the stable region of the disk. The fourth column is the SNR of GWB for LISA/Tianqin/Taiji.

where $\{e_p, f_p\}$ and $\{e(t=0), f_{\text{orb}}(t=0)\}$ are eccentricity and orbital frequency at plunge time and starting time, respectively. Then we evolve these new EMRIs $\{M_\bullet, m_{\text{sBH}}, z, e(t=0), f_{\text{orb}}(t=0)\}$ forward in time for the observation time T_{obs} of a space GW detection mission, and obtain $\{M_\bullet, m_{\text{sBH}}, z, e(t=T_{\text{obs}}), f_{\text{orb}}(t=T_{\text{obs}})\}$. It should be noted that $e(t=0) = e(t=T_{\text{obs}}) = 0$ for wet EMRI due to the strong circularisation.

Our result of the GWB in space-borne GW detector with $M_\bullet \in [10^4, 10^7]M_\odot$ contributed by the EMRIs in the universe (out to $z = 4.5$) is presented in Fig. 8, where we compare the GWB generated by the dry EMRIs and that generated by the wet EMRIs with different sBH accretion rate \dot{m}_{sBH} and the disk lifetime T_{disk} . The typical mission duration of the space-borne GW detectors is assumed to be 4 years, i.e., $T_{\text{obs}} = 4\text{yr}$. It should be noted that the setting of the SNR threshold of a single source will have a substantial impact on the GWB (see Bonetti & Sesana 2020) and we have subtracted GWs of individual sources with $S/N > 20$. The accretion of the sBH mostly affects the GWB spectrum at the sub-millihertz frequency region.

The observational effects of GWB contributed by the EMRIs have two different aspects. Firstly, this GWB could be a foreground noise that degrades the sensitivity for detecting some resolvable GW sources, in particular to the detectors such as LISA and Taiji when the accretion rate of sBH is relatively high as shown in Fig. 8. In this case, this GWB may be considered as unresolved background noise and the effective noise power spectral density can be estimated as $S_{\text{eff}}(f) = S_{\text{noise}}(f) + S_{\text{GWB}}(f)$, where is given by $S_{\text{GWB}}(f) = h_{c,\text{wet}}^2(f)/f$. For example, for an EMRI system with $M_\bullet = 10^6 M_\odot$, $m_{\text{sBH}} = 10 M_\odot$, eccentricity $e = 0$ and redshift $z = 0.2$. The accumulated SNR of the combined source after four years of observation to the final plunge is $\text{SNR} = (36, 16, 49)$ for (LISA, Tianqin, Taiji) for the model with the strongest GWB ($\dot{m}_{\text{sBH}} = 50\dot{M}_{\text{Edd}}$ and $T_{\text{disk}} = 5\text{Myr}$), while we have $\text{SNR} = (68, 20, 97)$ when the GWB is absented. Secondly, this GWB itself can be a targeted source carrying useful information about the galaxy centre environment. In this case, the detectability of the GWB is assessed by computing the associated power signal-to-noise ratio $(S/N)_{\text{dry/wet}}$ through (Thrane & Romano 2013; Sesana 2016)

$$(S/N)_{\text{dry/wet}}^2 = T_{\text{obs}} \int \gamma(f) \frac{h_{c,\text{dry/wet}}^4(f)}{f^2 S_{\text{noise}}^2(f)} df \quad (39)$$

where $S_{\text{noise}}(f)$ is the power spectral density of future space-borne GW detectors and the function $\gamma(f)$ is assumed to be approximately constant and equal to unity (see Thrane & Romano 2013). We list the SNR of dry and wet GWB in Table 1. All the models of wet EMRI

GWB listed in Table 1 have a significant signal-to-noise ratio and can be easily detected within 4 years of observation.

8 DISCUSSION AND CONCLUSIONS

In this work, we investigate the accretion effect on the distribution of stars and stellar mass black holes in the nuclear region surrounding the MBHs, by self-consistently evolving the extended Fokker-Planck equations. The time evolution of the distribution functions of the stellar mass black holes and stars are carefully analysed. We also study how the rate of the extreme-mass-ratio-inspiral events and their associated gravitational wave background is affected by the accretion effect. The observational consequences have also been presented in this work. (1) The accretion effect shifts the sBH distribution function over the mass to the heavier range, which will have effects on the future observations of stellar mass gravitational wave sources. Our analysis and estimation show that the mergers of sBHs, in particular those heavy sBHs with masses larger than 20 solar mass in the AGN accretion disk, could be an important component of the mass-distribution of the BBH merger events observed by the future 3rd generation ground-based gravitational wave detectors such as ET (Maggiore et al. 2020), Cosmic Explorer (Abbott et al. 2017). (2) On the aspect of space-borne gravitational wave detection, our work is relevant to the gravitational wave emitted from the EMRI systems. We found that the accretion effect has the possibility of degrading the detection of resolvable EMRI sources by a factor of $1.5 \sim 2$ via forming a stochastic gravitational wave foreground. Moreover, for the EMRI-generated gravitational wave background as the target source for future space-borne detectors, the accretion effect has only a minor effect on the signal-to-noise ratio.

However, the results presented in this work are still primitive. Many assumptions have been imposed in our modeling due to the complexity of the nuclear environment and the relevant physical processes, which are worth further discussions as follows.

Firstly, the damping timescale of orbiters' inclination is much shorter than the migration timescale only for low-inclination orbiters. For orbiters with high inclination angles, the dynamical friction (or the drag force) will dominate the damping process of the inclination angle, the timescale of which could be comparable to or longer than the migration time in disk (e.g., Cresswell & Nelson 2008; Rein 2012; Arzamasskiy et al. 2018; Zhu 2019; Nasim et al. 2022). In this case, the low-inclination orbiters (with inclination angle $i < \pi/4$, see Nasim et al. 2020; Fabj et al. 2020; Nasim et al. 2022) with shorter capture timescale will participate in the interaction with the disk (e.g. dynamic capture and scattering process) while the high-inclination ones with longer capture timescale remain in the cluster. Thus, the rates of replenishment of disk orbiters in this work are an upper limit since a significant fraction of orbiters with $i > \pi/4$ take significantly longer to be captured. In our calculation, the time average capture rate is obtained in the parameter $\mu_{\text{s}/\text{sBH}}$. One can phenomenologically treat the effects of different capture rates for these low- and high-inclination orbiters by adjusting the parameter $\mu_{\text{s}/\text{sBH}}$. It should be noted that, for numerical simplification, we still adopt the phenomenological treatment (Pan & Yang 2021a) for the disk capture process rather than calculate it from the first principle (Pan et al. 2022). The time-averaged wet EMRI rates by the phenomenological treatment are generally consistent with that from the first principle (see Pan et al. 2022).

Secondly, we did not include the migration process driven by dynamical friction in our calculation, which is also called type-0 migration (e.g., Syer et al. 1991; Vilkoviskij & Czerny 2002; Nasim et al.

2022; Paardekooper et al. 2022). The drag force is non-negligible when the mass ratio is small ($q \equiv m_{\text{sBH}}/M_{\bullet} < 10^{-7}$) and the gravitational interaction does not dominate (see Kley & Nelson 2012; Paardekooper et al. 2022, for reviews). For the EMRI system we focus on ($q \sim 10^{-6} - 10^{-3}$), the migration timescale and the capture timescale driven by density wave are several orders of magnitude shorter than that by dynamical friction for the low inclination orbiters (with orbital inclination angle $i < \pi/4$, see Cresswell & Nelson 2008; Rein 2012; Arzamasskiy et al. 2018; Fajj et al. 2020; Nasim et al. 2022). However, for the higher inclination and retrograde orbiters ($\pi/4 \leq i \leq \pi$), the dynamical friction will dominate the migration process and the damping of inclination angle, which will affect our results in two ways: (1) It can decrease the disk capture rate $\mu_{s/\text{sBH}}$ after the low inclination orbiters are depleted. One can relax this problem by adjusting the $\mu_{s/\text{sBH}}$. (2) It also affects the migration timescale of retrograde orbiters in the disk ($i = \pi$). The migration timescale of retrograde orbiters is about 5 – 10 times longer than that of prograde orbiters in disk ($i = 0$) (e.g., Secunda et al. 2021; Nasim et al. 2022), which could decrease the wet EMRI rate depending on the fraction of retrograde orbiters in the disk. However, in the disk, the fraction of retrograde orbiters could be much smaller than that of prograde orbiters because the stars/sBHs are mainly captured from the nuclear star cluster in active stage. For example, the simulation result in Arzamasskiy et al. (2018) showed that the capture timescale of low inclination orbiters in the prograde orbits ($i < \pi/4$) driven by density wave is 1-2 orders of magnitude shorter than that of retrograde orbiters ($\pi/2 < i < \pi$) driven by dynamical friction.

Thirdly, we also did not include the outward migration in our calculation (see Masset & Papaloizou 2003; Pepliński et al. 2008a,b; McKernan et al. 2011). The outward migration could occur when the star/sBH perturbs the disk, but is not strong enough to open a gap. The mass ratio q is about $10^{-5} - 10^{-4}$ for outward migration (McKernan et al. 2011) depending on the disk aspect ratio $h(r)$, surface density $\Sigma(r)$ and the viscous coefficient α , which generally need to be calculated by numerical simulation (Masset & Papaloizou 2003; Pepliński et al. 2008a,b). The outward migration could decrease the EMRI rate due to its fast runaway migration. However, sustaining this rapid mode of migration has proved to be very difficult, which strongly depends on the specific state of gas flow in the star/sBH's vicinity. For example, it needs a stringent condition such as a very steep positive surface density gradients in the disk (Pepliński et al. 2008a,b; Kley & Nelson 2012). Due to the stringent condition for the occurrence of the outward migration and the complexity of this issue, we temporarily did not consider the impact of outward migration in this work.

Fourthly, we adopted a fiducial model in this work, such as the total relative abundance of sBHs $\phi = 0.001$ and the fraction of AGN $f_{\text{wet}} = 1\%$. As shown in Fig. 8, the GWB of wet EMRI has a non-negligible impact on space-borne GW detectors, especially LISA/Taiji. It should be noted that the characteristic strain of GWB $h_{c,\text{wet}}^2 \propto \phi f_{\text{wet}}$, where wet GWB might have a stronger effect on the sensitivity curve with more sBHs and AGNs. In addition, the duty cycle of AGNs T_{disk} is still unclear. Estimated by the viscous timescale, the duty cycle is proportional to $\sqrt{M_{\bullet}}$ and is approximately in a range of $10^6 \sim 10^8 \text{yr}$ for $M_{\bullet} = 10^4 \sim 10^7 M_{\odot}$. However, the duty cycle is associated with many physical factors including gas supply and feedback process, etc. Here, we just take a homogeneous distribution of the duty cycle distribution $T_{\text{disk}} = \{5, 50\} \text{Myr}$ (e.g., Shulevski et al. 2015; Turner 2018) in this work.

Fifthly, the accretion process of stars/sBHs in the disk is quite unclear. We assume the accretion of sBHs is about $1\text{-}50 \dot{M}_{\text{Edd}}$ in

the stable region and \dot{M}_{Edd} in the unstable region (Yang et al. 2014; McKinney et al. 2014; Pan & Yang 2021b). For the accretion of stars, we take an empirical accretion model fitted from the universally high abundance ratio of [Fe/Mg] in the inner stable region (Toyouchi et al. 2022) and also assume the accretion rate is \dot{M}_{Edd} in the unstable region since the disk could be fragmentation and collapse into clumps. In addition, the evolution of stars in disk is also uncertain. We assume that stars with mass $50 M_{\odot} < m_s < 150 M_{\odot}$ will collapse into sBHs after 5 Myr (Toyouchi et al. 2022). During the active stage ($< 100 \text{Myr}$), fewer than 100 stars collapse into sBHs approximately, which has a small effect on the EMRI event rate, and mass distribution of sBH. However, in fact, the stars could have a higher accretion rate as shown in Wang et al. (2021); Cantiello et al. (2021); Dittmann et al. (2021); Jermyn et al. (2021), which indicates the possibility that more massive stars will collapse into sBHs.

Sixthly, the equation (26) and the associated parameters we used in the work is a simplified approximation. The binary mergers in the AGN accretion disk are also a complicated process that triggers many studies (e.g., Gröbner et al. 2020; Graham et al. 2020; Gerosa & Fishbach 2021; Li et al. 2022; Li & Lai 2022; Samsing et al. 2022). However, there are still many uncertain factors in the disc-binary interaction processes yet to be understood, which can affect our results of the dR/dm_{sBH} .

Seventhly, the binaries of stars/sBHs are not included in our calculation of the Fokker-Planck equations, which could have the following impact on our results. On one hand, the tidal capturing of one component in the binary could contribute to the EMRI rate (Hills 1988), which could be comparable to the EMRI rate driven by the two-body scattering (see Amaro-Seoane 2018, for a review). On the other hand, the dynamical effect of binaries (i.e., the three- and four-body encounters between binaries and single stars/binaries) may be important in the evolution of stars/sBHs' distribution function, which generally needs to be calculated by N-body or Monte Carlo simulations (e.g., Spurzem & Giersz 1996; Giersz & Spurzem 2000; Amaro-Seoane 2018). In this way, the EMRI rate may also be affected by the dynamical effect of binaries. These effects will be considered in the future work.

9 ACKNOWLEDGEMENTS

Y.M. thanks Professor Yanbei Chen for helpful discussions on the LIGO binary black hole detection, and Dr. Ning Jiang for the discussion on the AGN physics. He also thanks Professors Shun Wang and Jingtao Lü for useful conversations on non-equilibrium statistical physics. Q.W. thanks Professors Jianmin Wang and Luis C. Ho for the very useful discussions and comments on the disk stars. Y.M. is supported by the university start-up funding provided by Huazhong University of Science and Technology. M.W. and Q.W. is supported by the NSFC (grants U1931203, 12233007) and the science research grants from the China Manned Space Project (No. CMS-CSST-2021-A06). The authors acknowledge Beijing PARATERA Tech CO.,Ltd. for providing HPC resources that have contributed to the research results reported within this paper.

DATA AVAILABILITY STATEMENT: The data underlying this article will be shared on reasonable request to the corresponding authors.

APPENDIX A: DIFFUSION AND ADVECTION COEFFICIENTS IN THE FOKKER-PLANCK EQUATION

In this section, we extend the calculation of the diffusion and the advection coefficients of two-component (stars and sBHs with single mass) in [Pan & Yang \(2021a\)](#) to N-component (stars and sBHs with multiple mass) cases. We first define a few auxiliary functions:

$$\begin{aligned} F_0^i(m_i, E, r) &= (4\pi)^2 G m_i^2 \ln \Lambda \int_{-\infty}^E dE' \bar{f}_i(m_i, E'), \\ F_1^i(m_i, E, r) &= (4\pi)^2 G m_i^2 \ln \Lambda \int_E^{\phi(r)} dE' \left(\frac{\phi - E'}{\phi - E} \right)^{1/2} \bar{f}_i(m_i, E'), \\ F_2^i(m_i, E, r) &= (4\pi)^2 G m_i^2 \ln \Lambda \int_E^{\phi(r)} dE' \left(\frac{\phi - E'}{\phi - E} \right)^{3/2} \bar{f}_i(m_i, E'), \end{aligned} \quad (\text{A1})$$

where $i = \{\text{star, sBH}\}$, $\ln \Lambda$ the Coulomb's logarithm which take as $\ln \Lambda = 10$, and

$$\bar{f}_i(m_i, E') = \int_0^1 d\mathcal{R} f_i(E, \mathcal{R}, m_i). \quad (\text{A2})$$

With these auxiliary functions, the coefficients are written as

$$\begin{aligned} D_{EE}^i(E, \mathcal{R}, m_i) &= \frac{8\pi^2}{3} J_c^2 \int dm'_i \int_{r_-}^{r_+} \frac{dr}{v_r} v^2 \left[F_0^i(m'_i, E, r) + F_2^i(m'_i, E, r) \right], \\ &\quad + (i \leftrightarrow j), \\ D_E^i(E, \mathcal{R}, m_i) &= -8\pi^2 J_c^2 \int dm'_i \frac{m_i}{m'_i} \int_{r_-}^{r_+} \frac{dr}{v_r} F_1^i(m'_i, E, r) + \frac{m_i}{m_j} \times (i \leftrightarrow j), \\ D_{E\mathcal{R}}^i(E, \mathcal{R}, m_i) &= \\ &\quad \frac{16\pi^2}{3} J^2 \int dm'_i \int_{r_-}^{r_+} \frac{dr}{v_r} \left(\frac{v^2}{v_c^2 - 1} \right) \left[F_0^i(m'_i, E, r) + F_2^i(m'_i, E, r) \right] \\ &\quad + (i \leftrightarrow j), \\ D_{\mathcal{R}\mathcal{R}}^i(E, \mathcal{R}, m_i) &= \\ &\quad \frac{16\pi^2}{3} \mathcal{R} \int dm'_i \int_{r_-}^{r_+} \frac{dr}{v_r} \left\{ 2 \frac{r^2}{v^2} \left[v_t^2 \left(\frac{v^2}{v_c^2} - 1 \right) + v_r^2 \right] F_0^i(m'_i, E, r) \right. \\ &\quad \left. + 3 \frac{r^2}{v^2} v_r^2 F_1^i(m'_i, E, r) + \frac{r^2}{v^2} \left[2v_t^2 \left(\frac{v^2}{v_c^2} - 1 \right) - v_r^2 \right] F_2^i(m'_i, E, r) \right\} \\ &\quad + (i \leftrightarrow j), \\ D_{\mathcal{R}}^i(E, \mathcal{R}, m_i) &= -16\pi^2 \mathcal{R} r_c^2 \int dm'_i \frac{m_i}{m'_i} \int_{r_-}^{r_+} \frac{dr}{v_r} \left(1 - \frac{v_c^2}{v^2} \right) F_1^i(m'_i, E, r) \\ &\quad + \frac{m_i}{m_j} \times (i \leftrightarrow j), \end{aligned} \quad (\text{A3})$$

where $j = \{\text{star, sBH}\}$, $i \neq j$, and $v_t = J/r$ is the tangential velocity.

REFERENCES

Abbott B. P., et al., 2017, *Classical and Quantum Gravity*, **34**, 044001
 Abbott R., et al., 2020, *Phys. Rev. Lett.*, **125**, 101102
 Acernese F., et al., 2015, *Classical and Quantum Gravity*, **32**, 024001
 Amaro-Seoane P., 2018, *Living Reviews in Relativity*, **21**, 4
 Amaro-Seoane P., Preto M., 2011, *Classical and Quantum Gravity*, **28**, 094017
 Artymowicz P., 1993, *ApJ*, **419**, 166
 Arzamasov L., Zhu Z., Stone J. M., 2018, *MNRAS*, **475**, 3201
 Babak S., et al., 2017, *Phys. Rev. D*, **95**, 103012
 Barausse E., 2012, *MNRAS*, **423**, 2533

Belczynski K., Holz D. E., Bulik T., O'Shaughnessy R., 2016, *Nature*, **534**, 512
 Bellovary J. M., Mac Low M.-M., McKernan B., Ford K. E. S., 2016, *ApJ*, **819**, L17
 Binney J., Tremaine S., 2008, *Galactic Dynamics: Second Edition*
 Bonetti M., Sesana A., 2020, *Phys. Rev. D*, **102**, 103023
 Broggi L., Bortolas E., Bonetti M., Sesana A., Dotti M., 2022, *MNRAS*, **514**, 3270
 Cantiello M., Jermyn A. S., Lin D. N. C., 2021, *ApJ*, **910**, 94
 Chatterjee S., Rodriguez C. L., Rasio F. A., 2017, *ApJ*, **834**, 68
 Chattopadhyay D., Hurley J., Stevenson S., Raidani A., 2022, *MNRAS*, **513**, 4527
 Cohn H., 1979, *ApJ*, **234**, 1036
 Cohn H., Kulsrud R. M., 1978, *ApJ*, **226**, 1087
 Cresswell P., Nelson R. P., 2008, *A&A*, **482**, 677
 Derdzinski A., Mayer L., 2022, arXiv e-prints, p. arXiv:2205.10382
 Dittmann A. J., Cantiello M., Jermyn A. S., 2021, *ApJ*, **916**, 48
 Dotan C., Shaviv N. J., 2011, *MNRAS*, **413**, 1623
 Durisen R. H., Boss A. P., Mayer L., Nelson A. F., Quinn T., Rice W. K. M., 2007, in Reipurth B., Jewitt D., Keil K., eds, *Protostars and Planets V*. p. 607 (arXiv:astro-ph/0603179)
 Fabj G., Nasim S. S., Caban F., Ford K. E. S., McKernan B., Bellovary J. M., 2020, *MNRAS*, **499**, 2608
 Feng J., Cao X., Gu W.-M., Ma R.-Y., 2019, *ApJ*, **885**, 93
 Finn L. S., Thorne K. S., 2000, *Phys. Rev. D*, **62**, 124021
 Ford K. E. S., McKernan B., 2021, arXiv e-prints, p. arXiv:2109.03212
 Gerosa D., Fishbach M., 2021, *Nature Astronomy*, **5**, 749
 Giersz M., Spurzem R., 2000, *MNRAS*, **317**, 581
 Goldreich P., Tremaine S., 1978, *ApJ*, **222**, 850
 Goldreich P., Tremaine S., 1979, *ApJ*, **233**, 857
 Goldreich P., Tremaine S., 1980, *ApJ*, **241**, 425
 Graham M. J., et al., 2020, *Phys. Rev. Lett.*, **124**, 251102
 Graham M. J., et al., 2022, arXiv e-prints, p. arXiv:2209.13004
 Gröbner M., Ishibashi W., Tiwari S., Haney M., Jetzer P., 2020, *A&A*, **638**, A119
 Gu W.-M., 2012, *ApJ*, **753**, 118
 Gültekin K., et al., 2009, *ApJ*, **698**, 198
 Heger A., Woosley S. E., 2002, *ApJ*, **567**, 532
 Hills J. G., 1988, *Nature*, **331**, 687
 Hopman C., Alexander T., 2005, *ApJ*, **629**, 362
 Jermyn A. S., Dittmann A. J., Cantiello M., Perna R., 2021, *ApJ*, **914**, 105
 Kagra Collaboration et al., 2019, *Nature Astronomy*, **3**, 35
 Kennedy G. F., Meiron Y., Shukirgaliyev B., Panamarev T., Berczik P., Just A., Spurzem R., 2016, *MNRAS*, **460**, 240
 Kinugawa T., Nakamura T., Nakano H., 2021, *MNRAS*, **501**, L49
 Kley W., Nelson R. P., 2012, *ARA&A*, **50**, 211
 Kohler S., 2017, Are LIGO's Black Holes Made From Smaller Black Holes?, AAS Nova Highlight, 12 May 2017, id.2298
 Kormendy J., Ho L. C., 2013, *ARA&A*, **51**, 511
 LIGO Scientific Collaboration et al., 2015, *Classical and Quantum Gravity*, **32**, 074001
 Li J., Lai D., 2022, arXiv e-prints, p. arXiv:2211.07305
 Li Y.-P., Chen Y.-X., Lin D. N. C., Wang Z., 2022, *ApJ*, **928**, L1
 Lightman A. P., Shapiro S. L., 1977, *ApJ*, **211**, 244
 Lin D. N. C., Papaloizou J., 1986, *ApJ*, **309**, 846
 Loutrel N., 2020a, arXiv e-prints, p. arXiv:2009.11332
 Loutrel N., 2020b, *Classical and Quantum Gravity*, **37**, 075008
 Luo J., et al., 2016, *Classical and Quantum Gravity*, **33**, 035010
 Luo Z., Guo Z., Jin G., Wu Y., Hu W., 2020, *Results in Physics*, **16**, 102918
 Lyra W., Paardekooper S.-J., Mac Low M.-M., 2010, *ApJ*, **715**, L68
 MacLeod M., Lin D. N. C., 2020, *ApJ*, **889**, 94
 Macuga M., et al., 2019, *ApJ*, **874**, 54
 Maggiore M., et al., 2020, *J. Cosmology Astropart. Phys.*, **2020**, 050
 Magorrian J., Tremaine S., 1999, *MNRAS*, **309**, 447
 Mandel I., Farmer A., 2022, *Phys. Rep.*, **955**, 1
 Martini P., 2012, in American Astronomical Society Meeting Abstracts #220. p. 118.03
 Maset F. S., Papaloizou J. C. B., 2003, *ApJ*, **588**, 494

- McKernan B., Ford K. E. S., Lyra W., Perets H. B., Winter L. M., Yaqoob T., 2011, *MNRAS*, **417**, L103
- McKernan B., Ford K. E. S., Lyra W., Perets H. B., 2012, *MNRAS*, **425**, 460
- McKernan B., Ford K. E. S., Kocsis B., Lyra W., Winter L. M., 2014, *MNRAS*, **441**, 900
- McKernan B., et al., 2018, *ApJ*, **866**, 66
- McKinney J. C., Tchekhovskoy A., Sadowski A., Narayan R., 2014, *MNRAS*, **441**, 3177
- Merritt D., 2013, *Classical and Quantum Gravity*, **30**, 244005
- Nasim I., Gualandris A., Read J., Dehnen W., Delorme M., Antonini F., 2020, *MNRAS*, **497**, 739
- Nasim S. S., et al., 2022, arXiv e-prints, p. arXiv:2207.09540
- Nomoto K., Kobayashi C., Tominaga N., 2013, *ARA&A*, **51**, 457
- Paardekooper S. J., Baruteau C., Kley W., 2011, *MNRAS*, **410**, 293
- Paardekooper S.-J., Dong R., Duffell P., Fung J., Masset F. S., Ogilvie G., Tanaka H., 2022, arXiv e-prints, p. arXiv:2203.09595
- Pan Z., Yang H., 2021a, *Phys. Rev. D*, **103**, 103018
- Pan Z., Yang H., 2021b, *ApJ*, **923**, 173
- Pan Z., Lyu Z., Yang H., 2021, *Phys. Rev. D*, **104**, 063007
- Pan Z., Lyu Z., Yang H., 2022, *Phys. Rev. D*, **105**, 083005
- Panamarev T., Shukirgaliyev B., Meiron Y., Berczik P., Just A., Spurzem R., Omarov C., Vilkoviskij E., 2018, *MNRAS*, **476**, 4224
- Papaloizou J. C. B., 2021, in Madhusudhan N., ed., , *ExoFrontiers: Big Questions in Exoplanetary Science*. pp 13–1, doi:10.1088/2514-3433/abfa8fch13
- Peng P., Chen X., 2021, *MNRAS*, **505**, 1324
- Pepliński A., Artymowicz P., Mellema G., 2008a, *MNRAS*, **386**, 164
- Pepliński A., Artymowicz P., Mellema G., 2008b, *MNRAS*, **387**, 1063
- Peters P. C., 1964, *Physical Review*, **136**, 1224
- Rein H., 2012, *MNRAS*, **422**, 3611
- Robson T., Cornish N. J., Liu C., 2019, *Classical and Quantum Gravity*, **36**, 105011
- Salpeter E. E., 1955, *ApJ*, **121**, 161
- Samsing J., et al., 2022, *Nature*, **603**, 237
- Secunda A., Bellovary J., Mac Low M.-M., Ford K. E. S., McKernan B., Leigh N. W. C., Lyra W., Sándor Z., 2019, *ApJ*, **878**, 85
- Secunda A., et al., 2020, *ApJ*, **903**, 133
- Secunda A., Hernandez B., Goodman J., Leigh N. W. C., McKernan B., Ford K. E. S., Adorno J. I., 2021, *ApJ*, **908**, L27
- Sesana A., 2016, *Phys. Rev. Lett.*, **116**, 231102
- Shakura N. I., Sunyaev R. A., 1973, *A&A*, **24**, 337
- Shapiro S. L., Marchant A. B., 1978, *ApJ*, **225**, 603
- Shulevski A., et al., 2015, *A&A*, **583**, A89
- Sirko E., Goodman J., 2003, *MNRAS*, **341**, 501
- Spurzem R., Giersz M., 1996, *MNRAS*, **283**, 805
- Stone N. C., Metzger B. D., Haiman Z., 2017, *MNRAS*, **464**, 946
- Stone N. C., Generozov A., Vasiliev E., Metzger B. D., 2018, *MNRAS*, **480**, 5060
- Syer D., Clarke C. J., 1995, *MNRAS*, **277**, 758
- Syer D., Clarke C. J., Rees M. J., 1991, *MNRAS*, **250**, 505
- Tagawa H., Haiman Z., Kocsis B., 2020, *ApJ*, **898**, 25
- Tanaka H., Ward W. R., 2004, *ApJ*, **602**, 388
- Tanaka H., Takeuchi T., Ward W. R., 2002, *ApJ*, **565**, 1257
- The LIGO Scientific Collaboration et al., 2021a, arXiv e-prints, p. arXiv:2111.03606
- The LIGO Scientific Collaboration et al., 2021b, arXiv e-prints, p. arXiv:2111.03634
- Thrane E., Romano J. D., 2013, *Phys. Rev. D*, **88**, 124032
- Tiwari V., Fairhurst S., 2021, *ApJ*, **913**, L19
- Toyouchi D., Inayoshi K., Ishigaki M. N., Tominaga N., 2022, *MNRAS*, **512**, 2573
- Tremaine S., Richstone D. O., Byun Y.-I., Dressler A., Faber S. M., Grillmair C., Kormendy J., Lauer T. R., 1994, *AJ*, **107**, 634
- Tremaine S., et al., 2002, *ApJ*, **574**, 740
- Turner R. J., 2018, *MNRAS*, **476**, 2522
- Umeda H., Nomoto K., 2002, *ApJ*, **565**, 385
- Vilkoviskij E. Y., Czerny B., 2002, *A&A*, **387**, 804
- Wang J.-M., Liu J.-R., Ho L. C., Du P., 2021, *ApJ*, **911**, L14
- Ward W. R., 1997, *Icarus*, **126**, 261
- Yang X.-H., Yuan F., Ohsuga K., Bu D.-F., 2014, *ApJ*, **780**, 79
- Yang Y., et al., 2019a, *Phys. Rev. Lett.*, **123**, 181101
- Yang Y., Bartos I., Haiman Z., Kocsis B., Márka Z., Stone N. C., Márka S., 2019b, *ApJ*, **876**, 122
- Zhu Z., 2019, *MNRAS*, **483**, 4221
- van Son L. A. C., et al., 2022, *ApJ*, **940**, 184

This paper has been typeset from a $\text{\TeX}/\text{\LaTeX}$ file prepared by the author.